JOURNAL OF COMPUTATIONAL PHYSICS 80, 98–136 (1989)

A Computational Model Describing Confinement and Performance of Circular and D-Shaped Tokamak Plasmas

A. NICOLAI AND P. BÖRNER

Institut für Plasmaphysik der Kernforschungsanlage Jülich GmbH,
Association EURATOM-KFA, P.O.B. 1913,
D-5170 Jülich, Federal Republic of Germany

Received June 10, 1987; revised January 29, 1988

A combined one-dimensional and two-dimensional ("1 $\frac{1}{2}$ D") description of toroidal and axisymmetric plasmas is presented which is based essentially on an equilibrium solver resorting to the fast Buneman invertor ("equilibrium module") and two one-dimensional transport codes describing the protium, deuterium, tritium, and plasma energy inventory ("plasma module") and accounting for three impurity species ("impurity module"); it is employed to compute the time evolution of Tokamak plasmas. The attempt was made to achieve a consistent modelling of the transport and equilibrium phenomena in a plasma which interacts with the peripheral devices for, e.g., confinement, plasma heating, and limitation of the plasma aperture. The equilibrium solver is connected to a coil submodule computing the poloidal field coil currents maintaining the designed plasma shape approximately. A surface current density accounting for the magnetization of the iron core and the yokes is calculated by means of the module for the transformer iron. This module is linked to the equilibrium solver as well so that consistency between the coil currents, the plasma current distribution, and the magnetization of the transformer iron is achieved. The "scrape-off module" resorts to a radial model for the limiters. The modules for additional heating account for a full beam geometry within a simple approach for the RF-heating. The neutral atomic and molecular hydrogen species are described by a multidimensional Monte Carlo code or, alternatively, by the fast 1D-code SPUDNUT ("neutral gas module"). The MHD behaviour is estimated by evaluating the time evolution of the Mercier and the resistive interchange criteria ("stability module"). The calculations which are based on TEXTOR, JET, and INTOR data resort preferentially to the equilibrium, the coil, and the transformer module. It is shown that, e.g., in case of a specific shot, the measured-time evolution of the currents in the poloidal field coils of TEXTOR can be reproduced within an accuracy of 8%, only if the nonsaturated transformer iron is accounted for. The main results concerning JET and INTOR are: The performance of the JET-plasma is strongly influenced by the impurities essentially due to sputtering at the (noncarbonized) linear material (iron). The radiate 50% of the input power. These losses and the conduction losses limit the maximum plasma temperature at around 10 keV. Around the end of the discharge the transformer core is almost saturated and the nonsaturated yokes are important for the flux function distribution. The analysis of the INTOR-plasma shows that at a burn temperature $T_b = 10$ keV the fusion power (122 MW) exceeds the line radiation, ionization, conduction, and convection losses by 11 MW. Due to the high pressure gradient, the plasma turns out to be diamagnetic in the total cross section; the toroidal field, however, is reduced at the magnetic axis by 4% of the vacuum value only.

0021-9991/89 $3.00

1. INTRODUCTION

According to present theory of toroidal axisymmetric plasmas [1–7], the equilibrium quantities such as the toroidal and poloidal current densities and the correlated magnetic fields can be calculated self-consistently with the transport phenomena. The equilibrium quantities [8–12] are determined mainly by the poloidal field coil design, the plasma current, the pressure, and the q-profile; these profiles are provided by the transport processes in the central core. The energy inventory depends on the transport by conduction and convection, on radiation, and on the sources due to ohmic and additional heating by neutral injection, RF-heating methods, and fusion [3, 5, 10, 13–18]. The particle inventory emanates from sources controlled from the outside as pellet injection, gas puffing, neutral injection, and from the recycling processes, the perpendicular diffusion, and the parallel convection to the limiters or the divertor plates [19–22]. The hydrogen inventory in the first wall which is closely related to the recycling processes depends on the energy spectrum of the neutral particles, on the surface and bulk properties of the wall material, and might be comparable to or even larger than that of the plasma [23–25]. The transport phenomena listed above and the complex interaction of some of them had been treated analytically and numerically in many previous papers, e.g., [3, 5, 7, 14, 19].

During the time evolution of the discharge the flux surface geometry changes continuously, and in general no adiabatic variable is available among the commonly used parameters ψ (poloidal flux function), χ (toroidal flux function) and V (volume of the flux tube ψ). Therefore an iterative procedure consisting of a predictor step and a sufficient number of corrector steps [6] is to be applied in general. Hence the calculation iterates between the transport steps advancing the parameters ψ, χ, n_j (the densities, $j = 1, ..., 6$), T_e, and T_i (electron and ion temperatures) with respect to a fixed flux surface geometry, and the equilibrium steps updating the flux surface geometry and consequently the flux functions ψ and χ. The volume V changes according to the evolution of ψ and the parameters n_j, T_e, and T_i are advanced by adiabatic transformations. In this way, e.g., the dia- or paramagnetism of the plasma column and the temporal evolution of the equilibrium during adiabatic compression can be assessed. We note that in the examples just given, mainly the toroidal flux is affected. This confirms that χ cannot be treated as an adiabatic variable.

If flux-conserved states are reached, during which the q-profile is frozen in, the f-function, which is closely related to χ and therefore accounts also for the diamagnetic effects due to the increasing pressure, has to be computed consistently with $q(\psi)$ rather than prescribing it. Hence the equilibrium calculation iterates here between the Grad–Shafranov equation and an ordinary differential equation essentially needing the pressure and the q-profile as an input [3]. For the same reason, these profiles are chosen to link the transport and the equilibrium code [2, 3]. In this paper the plasma aperture is defined by limiters, and a possible separatrix is located beyond the outermost flux surface, therefore only closed flux surfaces are

available and the flux surface averages can be computed in the total plasma volume. In the case of divertor configurations the separatrix is to be excluded from the computation of the flux surface averages. As the limiting values just adjacent to the separatrix can be computed with sufficient accuracy, divertor configurations can be treated in principle by the same method to a good approximation. Nonsurface quantities such as the toroidal current density [10], which depend rather sensitively on the flux surface geometry and do not become frozen during flux-conserved states, are not envisaged here as a link between the transport and the equilibrium code.

Considerable progress [7] was achieved in the coupling of the Grad–Shafranov equation and the 1D-transport equations. In this approach mainly the voltages of the confining and magnetizing circuits, the geometry of the iron core for the transformer, and the power deposition profiles are used as an input. However, this procedure might yield unrealistic (hollow) plasma current distributions and it is difficult to maintain a prescribed plasma shape.

Instead of choosing the driving voltages as an input, in the following mainly the inverse problem is envisaged. At each equilibrium step the coil currents maintaining certain prescribed positions of the plasma boundary are computed iteratively by the coil submodule. In a predictor step this model estimates the coil currents by means of the surface current density in a dense coil fence [9] which shapes the plasma exactly. During the corrector steps the computed and the designed plasma shape are compared, and from the deviation of the two shapes in ψ-space the corrections of the coil currents are computed. The advantage of this procedure is that there are no restrictions concerning the coil positions. The vacuum magnetic field might be strongly distorted, if the transformer is equipped with an iron core [7]. Employing the discontinuity relation for the tangential component of the magnetic inductance an integral equation of Fredholm's second kind is derived for a surface current density, simulating the magnetic action of the iron. The computation of this current density is fast enough to be included in the iteration scheme of the equilibrium solver, so that consistency between the core's magnetization and the magnetic field generated by the plasma and the coils is achieved.

The advantages of the coupled code are:

1. The code is an extension of the 1D-radial transport code [23], the modules of which stay almost unchanged. These modules allow a detailed analysis of the charged and neutral particle densities, the energy inventory, and of the "q"-diffusion. In practice the degree of the coupling between the equilibrium and the transport calculation should be adjustable to the specific phase of the Tokamak operation, i.e., the heating, ignition, or burn phase. This can be achieved by changing the time interval between the equilibrium calls and by modifying the accuracy prescriptions. For some questions at hand a consistent plasma description is not necessary. In this case the modules can be used independently.

2. The expensive solution of the PDE and ODE concerns the rectangular domain containing the plasma only. The iron core and the coils are accounted for

by means of the boundary values which are to be imposed at the rectangular boundary. Thus a high resolution in the plasma domain is possible, which is needed for the stability analysis.

3. In the case of the free boundary value problem, briefly outlined in Section 6, the system of one-dimensional diffusion equations is restricted to the plasma volume. Outside the plasma zero-dimensional circuit equations resorting to the time centered inductivity matrix can be employed.

2. Computation of the Equilibrium Magnetic Fields and Current Densities inside the Plasma

The force densities due to the toroidal and poloidal current densities and the corresponding magnetic fields provide the plasma equilibrium [1–3, 7], the time evolution of which emanates from the resistivity, causing the "q diffusion" [3, 6] and the time dependence of the plasma pressure and of the coil currents. If the boundary values of the ψ-function (Sections 3, 5, or 6), the pressure, and the q-profile are provided, it is possible to compute the equilibrium quantities inside the plasma [2, 3]. There the magnetostatic equations can be combined to the Grad–Shafranov equation, a partial differential equation ("PDE")

$$\Delta^*\psi = -\mu_0 R^2 \frac{dp}{d\psi} - f\frac{df}{d\psi}. \tag{2.1}$$

The operator Δ^* is defined by

$$\Delta^* = R^2 \nabla \frac{1}{R^2} \nabla = \frac{\partial^2}{\partial R^2} + \frac{\partial^2}{\partial z^2} - \frac{1}{R}\frac{\partial}{\partial R}. \tag{2.2}$$

ψ is the poloidal flux function, μ_0 the vacuum permeability, p the pressure, and the f-function is defined by $f = \mu_0 R H_t$; R is the distance from the axis of symmetry, z the vertical coordinate (Fig. 1), H_t the toroidal magnetic field.

The PDE (2.1) is solved in a rectangular domain (Fig. 1) by means of the fast Buneman invertor [26]. This domain contains the plasma but not the coils or the iron core. The boundary values of the flux function are either prescribed at each iteration step as in the case of a fixed plasma boundary (Section 3) or computed from the coil currents and the plasma current distribution as in the case of the semi-free boundary (Section 5). As a flux surface average of the PDE (2.1) we obtain the ordinary differential equation ("ODE" [1, 2])

$$(K + Q^2/A)\psi'' + \left[K' + \frac{\mu_0 p}{\psi'^2} + \frac{Q}{A}\left(Q' - \frac{A'Q}{A}\right)\right]\psi' = 0 \tag{2.3}$$

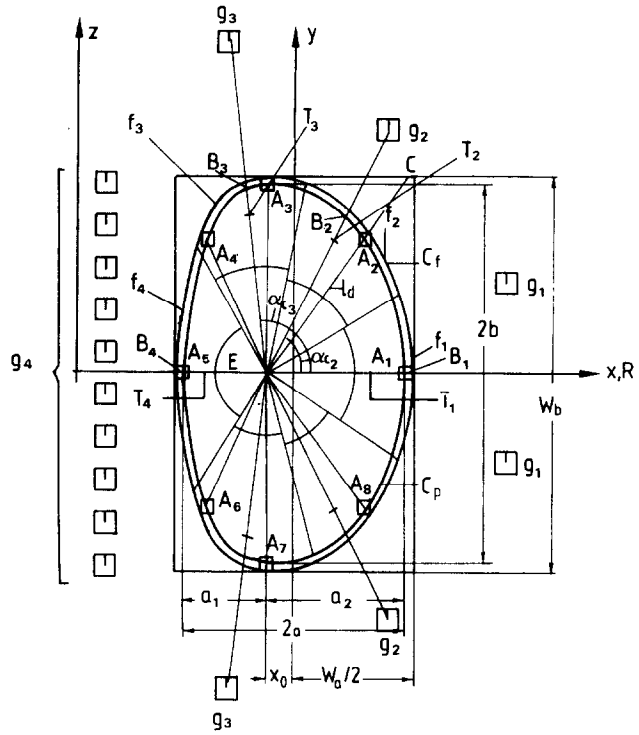

FIG. 1. Geometrical parametrization of the boundary C_p of a D-shaped axisymmetric plasma by the excentricity $e = a_2/a_1$, the ellipticity $\varepsilon = b/a$, the D-shape $d = l_d/a_2$ and the minor half-axis a. The plasma is surrounded by the coil fence C_f. The sectors f_i of this fence are assigned to each coil group g_i ($i = 1, ..., 4$). As specific examples the coil groups of JET are depicted, which are treated as a closed configuration. The distances of the points B_i, located on the designed plasma boundary, from the analogous points on the computed boundary are checked during the iteration in the flowchart of Fig. 2b. The points T_i are used as testpoints where the sectors of the coil fence and the corresponding coil groups generate the same flux function.

for the flux profile $\psi(V)$. The prime denotes the derivative with respect to the volume V,

$$K = \left\langle \frac{|\nabla\psi|^2}{R^2} \right\rangle_\psi \tag{2.4}$$

and

$$A = \left\langle \frac{1}{R^2} \right\rangle_\psi \tag{2.5}$$

are averages over the flux surface, $\psi = \text{const}$ [3]. The quantity Q is

$$Q = (4\pi)^2 q. \tag{2.6}$$

The solution method iterates between the PDE determining the geometry and the ODE (2.3) providing the flux profile, until convergence concerning the plasma current and the plasma shape is achieved.

During the iteration the minimum value of the flux function, $\psi(0)$ ("target value") is adjusted to account for the plasma current which is prescribed in the fixed boundary and semifree boundary value problem envisaged here. The plasma current is [2]

$$I_p = 2\pi R_0^2 \rho \left\langle \frac{|\nabla \rho|^2}{R^2} \right\rangle \tilde{H}_p(\rho)|_{\rho=\rho_p}; \tag{2.7}$$

R_0 is the distance of the magnetic axis from the axis of symmetry and ρ_p is the effective plasma radius; the analogous radius of an arbitrary flux surface is

$$\rho = \sqrt{V/2\pi^2 R_0} \tag{2.8}$$

and ρ_p is obtained from (2.8) with $V = V_p$, the plasma volume enclosed by the outermost flux surface. The quantity

$$\tilde{H}_p = \frac{1}{\mu_0} \frac{1}{R_0} \frac{\partial \psi}{\partial \rho} \tag{2.9}$$

is the effective poloidal field.

The new target value after the ith iteration step is

$$\psi^{(i+1)}(0) = -R_0 \frac{\tilde{\tilde{H}}_p^{(i)}(\rho_p)}{\tilde{H}_p^{(i)}(\rho_p)} \mu_0 \int \tilde{H}_p^{(i)} \, d\rho; \tag{2.10}$$

$\tilde{H}_p^{(i)}$ is the field after the ith iteration and $\tilde{\tilde{H}}_p^{(i)}(\rho_p)$ is the boundary value according to Eq. (2.7) with the most recent average value

$$\left\langle \frac{|\nabla \rho|^2}{R^2} \right\rangle_\psi = \frac{K}{(\mu_0 \tilde{H}_p R_0)^2}. \tag{2.11}$$

The iteration according to (2.10) ensures that the current I_p given by Eq. (2.7) approaches the prescribed value step by step. Convergence concerning the plasma current is achieved if

$$\text{Max}\left[\frac{|I_p - I_d|}{I_d}, \frac{|I_p' - I_d|}{I_d} \right] < \varepsilon_1. \tag{2.12}$$

J_p is defined by Eq. (2.7) with the most recent values of all quantities involved there, J_p' is the plasma current computed from the two-dimensional current distribution

$$j_t(R, z) = \frac{1}{R\mu_0} \Delta^* \psi = -R \frac{dp}{d\psi} - \frac{1}{R\mu_0} f \frac{df}{d\psi}. \tag{2.13}$$

I_d is the prescribed plasma current and ε_1 is a prescribed accuracy parameter ($\varepsilon_1 = 1\%$ in Section 10). The computation of the boundary values for the PDE and the convergence check concerning the plasma shape depend on the specific problems to be solved. These are discussed in the Sections 3, 5, and 6.

2.1. *Local and Global Pressure Balance*

The accuracy of the equilibrium calculation may be checked by the local and global pressure balances which are

$$j_t(R, z)\, H_p(R, z) = -\frac{1}{\mu_0} \nabla p + j_p(R, z)\, H_t(R, z) \tag{2.1.1}$$

and

$$\tilde{H}_p(\rho)\, \tilde{j}_t(\rho) = -\frac{1}{\mu_0} \frac{\partial p}{\partial \rho} + \tilde{j}_p(\rho)\, \tilde{H}_t(\rho), \tag{2.1.2}$$

respectively.

The poloidal field H_p, the poloidal current density j_p and the toroidal field H_t are given by

$$H_p(R, z) = \frac{|\nabla \psi|}{R \mu_0} \tag{2.1.3}$$

$$j_p(R, z) = -\frac{1}{\mu_0} \frac{\partial f}{\partial \psi} \frac{|\nabla \psi|}{R} \tag{2.1.4}$$

and

$$H_t = \frac{f(\psi)}{R \mu_0}. \tag{2.1.5}$$

The analogous effective toroidal field $\tilde{H}_t$ and the current densities $\tilde{j}_p, \tilde{j}_t$ are given by

$$\tilde{H}_t = \frac{1}{\mu_0 \rho} \frac{\partial \chi}{\partial \rho} \tag{2.1.6}$$

$$\tilde{j}_p = \frac{1}{2\pi R_0} \frac{\partial I_{\text{pol}}}{\partial \rho} \tag{2.1.7}$$

$$\tilde{j}_t = \frac{1}{2\pi \rho} \frac{\partial I_{\text{tor}}}{\partial \rho}. \tag{2.1.8}$$

They depend on the flux surface label ρ only; p stands for "poloidal," and t for "toroidal." χ is the toroidal flux function. The toroidal current I_{tor} and the poloidal current I_{pol}, both within the flux surface ρ, are

$$I_{\text{tor}}(\rho) = 2\pi \rho R_0^2 \left\langle \frac{|\nabla \rho|^2}{R^2} \right\rangle \tilde{H}_p(\rho) \tag{2.1.9}$$

and

$$I_{\text{pol}} = \frac{2\pi}{\mu_0}(f_0 - f) = 2\pi\left(R_0 H_{t_0} - \frac{1}{R_0 A}\tilde{H}_t(\rho)\right). \tag{2.1.10}$$

(2.1.9) is a generalization of Eq. (2.7). The index "0" denotes the magnetic axis. To simplify the notation besides the magnetic fields H_p, H_t, $\tilde{H}_p$, and $\tilde{H}_t$, the corresponding inductions B_p, B_t, $\tilde{B}_p$, and $\tilde{B}_t$ are introduced in the following and may be used in the preceding equations as well.

We note that in low β cases the pressure gradient is small compared to the $j \times B$-force densities. Comparing ∇p with the difference of the $j \times B$-force densities might reveal a large inaccuracy not inherent to the calculation. This can be avoided by combining the pressure gradient with one of $j \times B$-force densities, as in Eq. (2.1.1) or (2.1.2). The LHS and RHS of Eq. (2.1.1) and (2.1.2) were computed in the case of specific examples given in Section 10. These show that the relative deviations between the respective maximum force densities are less than 2%.

2.2. *Time-Step Control*

The time step $(\Delta t_{is})_n$ between the $(n-1)$th and the nth equilibrium call (Section 8) can be predicted by means of the pressure and q-changes between these calls; $(\Delta t_{is})_n$ reads

$$(\Delta t_{is})_n = \text{Min}\left[(\Delta t_{is})_{n-1}\frac{\gamma}{\alpha_t + 0.01\gamma}, \Delta t_{is_{\max}}\right]$$

with

$$\alpha_t = \text{Max}\left[\frac{q_n(\rho) - q_{n-1}(\rho)}{0.5(q_n(\rho) + q_{n-1}(\rho))}, \frac{p_n(\rho) - p_{n-1}(\rho)}{0.5(p_n(\rho) + p_{n-1}(\rho))}\right].$$

$\Delta t_{is_{\max}}$ is a prescribed upper limit (= 100 ms). If the ODE–PDE iteration fails to converge, the time step is repeated with one-half of its original value. $(\Delta t_{is})_0 =$ 10 ms is prescribed.

3. Fixed Boundary Value Problem

The "fixed boundary" version of the equilibrium module computes a plasma equilibrium belonging to a prescribed D-shaped boundary. A rectangle (Fig. 1) is used as the mathematical boundary. W_a and W_b are the rectangle's width and height, respectively. It is convenient for the following to use a cartesian coordinate system (x, y) anchored in the center of the rectangle. The flux function $\psi(x, y)$ is prescribed on the rectangular boundary such that the plasma edge $\psi = 0$ agrees with the designed plasma within a given accuracy limit ε_2 (Eq. 3.10).

As the pressure and q-profile evolve in time these boundary values have to be

adjusted at each call of the equilibrium code to maintain the same plasma shape. Here a D-shaped plasma cross section (Fig. 1) is defined by its horizontal extension $2a$, the ellipticity $\varepsilon = b/a$ ($2b$ is the vertical extension), the excentricity $e = a_1/a_2$, and the D-shapeness $d = l_d/a_2$. a_2 and a_1 are given by the straight line connecting the maximum A_3 with the minimum A_7. l_d is the part EA_2 of the straight line connecting the point E with the rectangle's corner C.

Here two analytical options are available to describe the designed plasma shape. The first uses the foregoing shape parameters directly, the second employs them indirectly to compute the parameters of a closed representation of the plasma boundary.

Two composed ellipses with the major semiaxis b in common and different minor semiaxis a_1, a_2 are used in the case of the first option; i.e., the plasma boundary is given by the expressions

$$\begin{aligned} \left(\frac{x-x_0}{a_1}\right)^2 + \left(\frac{y}{b}\right)^2 &= 1 \qquad \frac{W_a}{2} \leqslant x \leqslant x_0 \\ \left(\frac{x-x_0}{a_2}\right)^2 + \left(\frac{y}{b}\right)^2 &= 1 \qquad x_0 \leqslant x \leqslant \frac{W_a}{2}, \end{aligned} \tag{3.1}$$

where the origin of the cartesian coordinate system coincides with the center of the circumscribed rectangle. x_0 is the distance of the common center of the ellipses from the origin 0. The plasma radius ρ_p is

$$\rho_p = \sqrt{ab}. \tag{3.2}$$

The main drawback of the foregoing definition is that the D-shapeness d cannot be prescribed independently; it is connected to the other parameters by

$$d = \sqrt{\left(1 + \varepsilon^2 \frac{(e+1)^2}{4e^2}\right)} \Big/ 2. \tag{3.3}$$

Furthermore, the curvature of the boundary changes discontinuously.

The second option uses the analytical expression [11]

$$\left(\frac{x'}{a_c}\right)^2 + \left(\frac{y'}{b_c}\right)^2 - \frac{\tau_t}{a_c^3}(x'^3 - 3x'y'^2) + \frac{\tau_q}{a_c^4} x'^4 y'^4 = 1. \tag{3.4}$$

The local system (x', y') is connected to the system (x, y) of Fig. 1 by $y' = y$, $x' = x - x_1$.

By the choice of x_1 the boundary is centered within the rectangle. The quantities a_c, b_c, the "triangularity" τ_t and the "quadrangularity" τ_q are computed such that the boundary defined by Eq. (3.4) has a prescribed vertical extension $2b$, horizontal extension $2a$, excentricity e, and D-shapeness d.

The boundary values for the ψ-function on the rectangle are computed from the analytical expression

$$\psi_b(x, y) = F(x, y) + \beta(x, y) + \gamma(x, y) + \psi_1. \tag{3.5}$$

The functions F, β, and γ are

$$F(x, y) = \begin{cases} g_1(x, y, x_0, a_1, b, r_1)\alpha_1, & x \in \xi_1;\ y \in \eta \\ g_1(x, y, x_0, a_2, b, r_1)\alpha_2, & x \in \xi_2;\ y \in \eta \end{cases} \tag{3.6}$$

$$\beta(x, y) = \begin{cases} 0, & x = -W_a/2;\ y \in \eta \\ g_2(y, b, r_1/2)\psi_2, & x = W_a/2;\ y \in \eta \\ 0, & x \in \xi_1 + \xi_2;\ y = \pm W_b/2 \end{cases} \tag{3.7}$$

$$\gamma(x, y) = \begin{cases} g_3(x, a_1, r_2)\psi_3, & x \in \xi_1;\ y = \pm W_a/2 \\ g_3(x, a_2, r_3)\psi_3, & x \in \xi_2;\ y = \pm W_b/2 \\ 0, & x = \pm W_a/2;\ y \in \eta. \end{cases} \tag{3.8}$$

The functions g_1 and g_2 are defined by

$$g_1(x, y, x_0, a^*, b^*, r) = \left[\left(\frac{x - x_0}{a^*}\right)^2 + \left(\frac{y}{b^*}\right)^2\right] \Big/ r^2 - 1$$

$$g_2(y, b^*, r) = [r^2 - (y/b^*)^2]/r^2$$

$$g_3(x, a^*, r) = [r^2 - (x - x_0)^2/a^{*2}]/r^2$$

and the geometrical parameters r_1, r_2, and r_3 are

$$r_1 = W_b/b$$

$$r_2 = (-W_a/2 - x_0)/a_1$$

$$r_3 = (W_a/2 - x_0)/a_2.$$

The intervals ξ_1, ξ_2, and η are given by

$$\xi_1 \equiv [-W_a/2, x_0], \qquad \xi_2 \equiv [x_0, W_a/2]$$

$$\eta \equiv \left[-\frac{W_b}{2}, \frac{W_b}{2}\right].$$

We note that in [5] an expression similar to (3.5), suited for circular plasmas, was given. α_1 and α_2 account for the deformation; ψ_1, ψ_2, and ψ_3 are used to center the plasma within the rectangle.

During the iteration between the PDE and the ODE the parameters α_1, α_2, ψ_1,

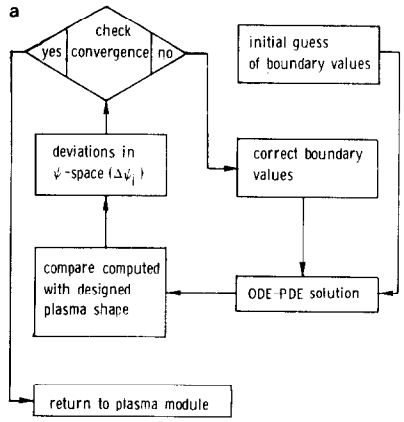

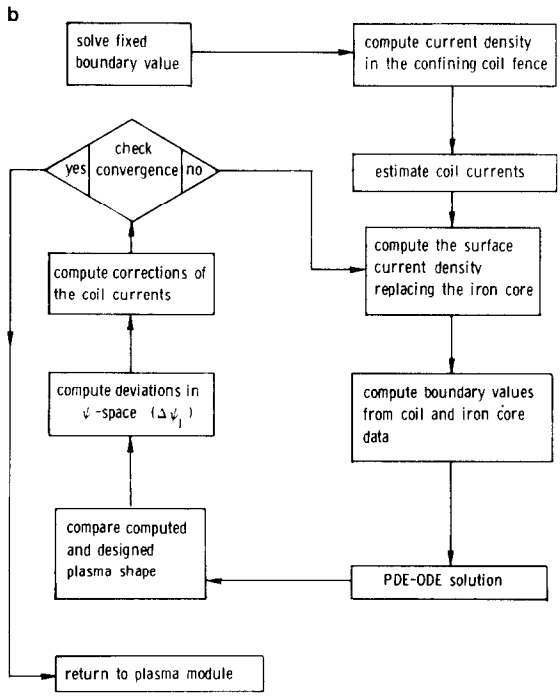

FIG. 2. Flow charts for the fixed (a) and semifree (b) boundary value problems. In (a) at each step of the ODE–PDE iteration, the designed and computed plasma boundaries are compared and the boundary values are corrected accordingly. In (b) the coil currents are adjusted iteratively to meet a prescribed boundary at specific points. The mirror current density replacing the transformer iron is computed at each iteration step.

ψ_2, ψ_3 are adjusted such that the plasma edge $\psi = 0$ fits the prescribed boundary at 8 points $A_{1\ 8}$ shown in Fig. 1 within a prescribed accuracy.

Let $((x_{p_i}, y_{p_i})$, $i = 1, ..., 8)$, be the coordinates of the intersection points of the plasma boundary with the 8 straight lines $EA_{1\ 8}$ and $((x_{L_i}, y_{L_i})$, $i = 1, ..., 8)$ the analogous coordinates of the designed positions $A_{1\text{-}8}$. The corrections $\Delta\alpha_1$, $\Delta\alpha_2$, $\Delta\psi_{1\ 3}$ for the next iteration step are

$$\begin{aligned}
\Delta\psi_1 &= F_{\psi_1} \cdot (\psi(x_{p5}, y_{p5}) - \psi(x_{L5}, y_{L5})) \\
\Delta\psi_2 &= F_{\psi_2} \cdot (\psi(x_{p_1}, y_{p_1}) - \psi(x_{L_1}, y_{L_1})) \\
\Delta\psi_3 &= F_{\psi_3} \cdot (\psi(x_{p_3}, y_{p_3}) - \psi(x_{L_3}, y_{L_3})) \\
\Delta\alpha_1 &= F_{\alpha_1} \cdot (\psi(x_{p4}, y_{p4}) - \psi_{L4}, y_{L4})) \\
\Delta\alpha_2 &= F_{\alpha_2} \cdot (\psi(x_{p_2}, y_{p_2}) - \psi(x_{L_2}, y_{L_2})).
\end{aligned} \tag{3.9}$$

The correction factors $F_{\psi_{1\text{-}3}}$ and $F_{\alpha_{1,2}}$ are of the order of unity. By optimizing these factors it can be shown that in the case of INTOR and JET, convergence (defined below) can be achieved within 20 iteration steps if $F_{\psi 1} = 1$, $F_{\psi 2} = 1$, $F_{\psi 3} = 1.5$, $F_{\alpha_1} = 0.4$, $F_{\alpha_2} = 0.6$ are chosen.

The iteration is stopped if the conditions for the relative deviations

$$\frac{\Delta l_i}{l_i} = \sqrt{\frac{(x_{p_i} - x_{L_i}) + (y_{p_i} - y_{L_i})^2}{x_{p_i}^2 + y_{p_i}^2}} < \varepsilon_2, \qquad i = 1, ..., 8 \tag{3.10}$$

($\varepsilon_2 = 1\,\%$ in case of the fixed boundary value problem) are fulfilled.

Although the other points of the boundary are not checked during the iteration, the computed boundary agrees well with the designed boundary if convergence is achieved for the eight points only (see Section 10).

We note that the solution of the Grad–Shafranov equation (2.1) by a finite element solver might be superior to the method just described because the plasma boundary can be prescribed directly so that convergence concerning the plasma shape needs not be checked. However, in the case of the semifree boundary value problem, in which ψ_b is computed from the coil currents and the plasma current distribution, an analogous procedure is chosen to obtain the coil currents iteratively. Hence the procedure used here is a first step for the treatment of the semifree boundary value problem (Section 5). The flowchart of the equilibrium solver for the fixed value problem is given in Fig. 2a.

4. Confining Coil Fence

To predict the coil currents of the closed configurations (Section 5.2) the current density j_c in the confining "dense" coil fence is (Fig. 1) needed. This current density in the fence surrounding the plasma and maintaining the plasma shape can in

principle be calculated from the condition that the flux function vanishes at the plasma edge. This condition reads

$$\int_{C_f} dl_f j_f(x_f y_f)\, C(x, y; x_f y_f) + \int_{V_p} j_p(x_p, y_p)\, C(x, y; x_p, y_p)\, dx_p\, dy_p = 0 \tag{4.1}$$

and is an integral equation for $j_f(x_f, y_f)$.

The ranges of integration belonging to the 1st and 2nd integral in Eq. (4.1) are the curve C_f defined by the coil fence and the plasma volume V_p, respectively (Fig. 1). (x, y) denote the test points at the plasma edge, (x_f, y_f) the source points on C_f, dl_f the line element of C_f, and (x_p, y_p) the source points inside the plasma volume. $C(x, y; x_p, y_p)$ is essentially the vector potential of a circular conductor [9] and $j_p(x_p, y_p)$ is the density of the toroidal plasma current.

To avoid the singularity of $C(x, y; x_p, y_p)$ occurring for $(x, y) = (x_p, y_p)$, the curve for the test points is shifted away from the plasma edge by a small distance; consequently the left-hand side of Eq. (4.1) must be replaced by $\psi(x, y) > 0$.

By integrating the current distribution in the sectors f_j defined by the coil position (Fig. 1), approximations of the coil currents can be obtained if the coils are located in the vicinity of the fence. These currents are used for starting the iteration of the semifree boundary value problem (Section 5).

Employing Gauss integration in Eq. (4.1) with a node number $N_{FC} \approx 75$ a linear system of equations is obtained which is solved by a standard procedure for matrix inversion. To obtain a stable solution the node density must be rather high.

By introducing, e.g., normalized Legendre polynomials as an orthonormal basis equation (4.1) can be rewritten analogously to the procedure used in Section 7 as a system of linear equations. The rank of the system matrix is truncated at a number N_L, which emanates from the accuracy requirements.

As j_f is used to obtain an estimate of the coil currents, $N_L = 10$ is in general sufficient. Thus the rank of the matrix needed to solve (4.1) in configuration space is strongly reduced.

We note that the volume integral in Eq. (4.1) can be replaced by a surface integral over a current density j_{vc} which is proportional to the poloidal field at the plasma boundary [9] ("virtual casing"). It follows from Eq. (4.1) that j_f becomes equal to j_{vc} if the plasma boundary and the coil fence almost coincide. This can be used as a check.

5. Semifree Boundary Value Problem

Instead of adjusting the shaping parameters of Eq. (3.6)–(3.8) in this section, the coil currents are computed iteratively under the condition that the plasma boundary reaches certain prescribed positions within prescribed error limits. By repeating

this procedure at each equilibrium call the time evolution of the coil currents shaping and centering the plasma is obtained. This does not include the currents in the feedback system which are to be controlled on the millisecond time scale to cope, e.g., with the fast β_p changes due to the tearing mode activity and with the vertical position instability.

In the transport part of the code (Section 8) it is attempted to account only for the time-averaged effects of the instabilities by employing phenomenological transport coefficients. Therefore the coil currents obtained here are time-averaged values as well, corresponding to the mean β_p values.

By assuming top–bottom symmetry the vertical instability is excluded from consideration here. Three coil configurations are envisaged:

1. The "open" configuration; mainly two coils as indicated in Fig. 3 are employed to confine an almost circular plasma.

2. The "closed" configuration (Fig. 1) which is related to the confining coil fence of Section 4.

3. The "mixed" configurations which may engender noncircular plasmas as the closed configurations and resort to more than one coil group for plasma shaping.

If the equilibrium is to be calculated from given coil currents, as in the free boundary value problem (Section 6), the open, the closed, and the mixed configurations can be treated in the same way. In the semifree boundary value problem, however, the treatment of the open and mixed configurations differs from that of the closed configurations because the plasma volume is to be defined by a special procedure for solving the ODE.

5.1. *Open Configurations*

The starting point is that a circular plasma can be confined by a homogeneous vertical field. This field may be generated approximately by a combination of two

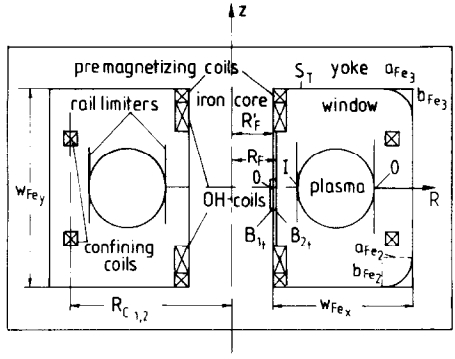

FIG. 3. Open configuration (TEXTOR) with iron core yokes and poloidal field coils. The parametrization of the window's inner boundary resorts to the lengths w_{Fe_y}, w_{Fe_x}, a_{Fe_j}, b_{Fe_i} $(i = 1, ..., 4)$ and ensures that the normal vector of this boundary changes continuously.

coils at radius R_c as shown in Fig. 3. This figure depicts the iron core and the yokes; the parametrization of the inner boundary of the iron domain is given as well. Here we concentrate on the action of the poloidal field coils. The influence of the iron will be discussed in Section 7.

As in the case of the closed configurations (Section 5.2) the coil currents are predicted by means of the fixed boundary version of the code for a circular plasma ($\varepsilon = d = e = 1$). After computing the pressure and the q profile from the initial conditions for the transport part of the code (Section 8), the confining vertical field H_v is computed from the ψ-function of the coil fence. The predictor value of J_c emanates from the condition that the vertical component of the coils' field at the plasma center equals H_v. From the positions of the outer limiter's edge $(x_{L_1}, 0)$ and the plasma edge $(x_{p_1}, 0)$ the corrections of the coil currents

$$\Delta I_{C_1} = \frac{0.5(\psi(x_{p_1}, 0) - \psi(x_{L_1}, 0))}{C(x_{C_1}, 0; x_{L_1}, 0)} \tag{5.1.1}$$

are computed (Fig. 2b). x_c is the abscissa of the coils' center. From the analogous positions of the inner plasma edge $(x_{p_5}, 0)$ and the inner limiter edge $(x_{L_5}, 0)$, the correction of the plasma volume $\Delta V_p = 4\pi^2 R_0 a(x_{L_5} - x_{p_5})$, and by linear interpolation ($\Delta V_p < 0$) or extrapolation ($\Delta V_p > 0$), the corresponding correction of the flux function at the boundary

$$\Delta\psi = P_L\{[\boldsymbol{\psi}, \mathbf{V}], V_{N_V} + \Delta V_p\} \tag{5.1.2}$$

can be computed. $\mathbf{V}$ denotes the nodes V_j for the ODE-integration and $\boldsymbol{\psi}$ the ψ_j-values ($j = 1, ..., N_v$) computed by the preceding iteration step, and P_L the linear inter- (or extra-) polation. By means of a new equidistant grid between 0 and $V_{N_v} + \Delta v_p$, all one-dimensional quantities needed for the integration of the ODE are newly interpolated from the old ones. The iteration is then continued with the integration of the ODE.

Although the boundary has to meet prescribed positions only at two points, the calculations show (Section 10) that it is almost circular, even if the iron core is taken into account. During the time evolution of the discharge, the boundary is free except at the prescribed positions. Convergence is achieved if the condition (2.12) and the condition (3.10) for $i = 1$ and $i = 5$ are fulfilled. The OH-coils (Fig. 3) mainly influence the magnetization of the iron core (Section 7), thereby providing the flux swing necessary to drive the plasma current.

5.2. *Closed Configurations*

In the case of closed configurations the coils surround the plasma as shown in Fig. 1 for the poloidal field coils and the primary solenoid of JET. The coil currents are predicted and corrected during the ODE–PDE iteration until convergence concerning the plasma current and the plasma shape is achieved. For simple technical reasons a realization of the coil fence which is needed to match an arbitrarily

designed plasma boundary exactly is not possible. Therefore deviations between the plasma shape designed, e.g., according to (3.1) or (3.4) and the shape computed by the subsequent procedure will occur if realistic coil data are employed.

The coils belong in general to coil groups which are assumed here to be connected in series. In the case of a D-shaped plasma, four independent groups g_1–g_4 (containing at least one coil) indicated in Fig. 1 are envisaged to adjust the minor axis a, the elongation, and the D-shapeness and to center the plasma radially. If these coil groups cannot be operated independently, as in the case of JET, at least two of the shaping parameters will be coupled because the ratio of the currents in the coils operated in series stays constant.

It is assumed here that the primary solenoid can be treated as a poloidal field coil

The meaning of this assumption for, e.g., JET discharges is discussed in Section 5.3.

In case of the open configurations only one coil group was used to position the outer plasma edge; here each coil group is employed to influence the "opposite" part of the plasma contour. This presupposes that the coils are located in the vicinity of the plasma boundary, i.e., between the vacuum vessel and the toroidal field coils.

The "stiff" configurations as in case of INTOR [27] are excluded from the considerations given below because the distance between the coils and the plasma boundary is large.

By intersecting the straight lines $EB_j\, j = 1, ..., N_G$ (Fig. 1) with the computed and the designed plasma periphery, which might be described by Eq. (3.1) or (3.4), the positions are obtained where during the PDE–ODE iterations both contours are to be compared. N_G is the number of the coil groups.

The analogous positions at the coil fence (Fig. 1) are used to obtain the first approximation of the coil currents for the predictor step. The part of the coil fence alloted to each coil group is indicated in Fig. 1 ("f_1–f_4"). As the coil fence is located in the vicinity of the plasma boundary and the coils are more remote from the plasma periphery, the currents

$$I_{f_j} = \int_{l_{j-1}}^{l_j} dl j_c(l) \tag{5.2.1}$$

are rescaled according to

$$I_{f_j'} = \frac{C(X_{T_j}, Y_{T_j}, X_{B_j}, Y_{B_j})}{C(X_{T_j}, Y_{T_j}, X_{C_j}, Y_{C_j})} I_{f_j}. \tag{5.2.2}$$

Here as in the following, the index $j = 1, 2, ..., N_G$ stands for the coil groups. l_j is the arc length of the coil fence at the end of each sector f_j, (x_{c_j}, y_{c_j}) are the coordinates of the coil positions, (x_{T_j}, y_{T_j}) are the coordinate of the test points T_j indicated in Fig. 1, and (x_{B_j}, y_{B_j}) are the coordinates of the points B_j.

From the differences

$$\Delta\psi_j = \psi(X_{p_j}, Y_{p_j}) - \psi(X_{L_j}, Y_{L_j}), \qquad j = 1, ..., 8, \tag{5.2.3}$$

which are computed as in case of the fixed boundary value problem, the analogous deviations $\overline{\Delta\psi_j}$, defined by means of the points B_j, are calculated by an interpolation P_S,

$$\overline{\Delta\psi_j} = P_S[\{\Delta\boldsymbol{\psi}, \boldsymbol{\alpha}_p\}, \alpha_{c_j}\}, \qquad j = 1, ..., N_G; \tag{5.2.4}$$

$\Delta\boldsymbol{\psi}$ denotes the array (5.2.3) and $\boldsymbol{\alpha}_p$ the set of the angles belonging to the points A_j (Fig. 1); α_{c_j} is the angle of the coil group j. Analogously to Eq. (4.1.1) the corrections of the coil group currents read

$$\Delta J_{cj} = \begin{Bmatrix} \mathrm{Min}(\Delta J'_{cj}, \Delta J_L); \Delta J'_{cj} > 0 \\ \mathrm{Max}(\Delta J'_{cj}, -\Delta J_L); \Delta J'_{ci} < 0 \end{Bmatrix} \tag{5.2.5}$$

with

$$\Delta J'_{cj} = F_{cj}\, \Delta_{\psi j}/C(x_{cj}, x_{cj}; x_{Bj}, y_{Bj}), \qquad j = 1, ..., N_G. \tag{5.2.6}$$

In contrast to the corrections (3.9) in case of the fixed boundary, the change of each coil current influences the total plasma boundary in principle so that the corrections are not independent. Essential for convergence is the proper choice of the factor F_{cj} and of the upper and lower limits $= \pm \Delta J_L$ for the corrections ΔJ_{cj}.

The factors F_{cj} account for the fact that the part of the plasma contour shaped mainly by coil group j might overlap with that part shaped by the group $j \pm 1$. Examples are the coils g_2 and g_3 in Fig. 1. For the D-shaped plasma of Fig. 1, $F_{c_1} = 2$, $F_{c_2} = 0.3$, $F_{c_3} = 0.3$, $F_{c_4} = 3$, were chosen. For stiff configurations the overlapping is so strong that the procedure breaks down. The iteration is stopped if (2.12) with $\varepsilon_1 = 1\,\%$ and the conditions (3.10) with $\varepsilon_2 = 2\,\%$ are fulfilled. Compared to the fixed boundary values problem the accuracy prescription is somewhat relaxed.

In this case a maximum number of iterations $N_{it} = 50$ turns out to be sufficient. If convergence cannot be achieved for a prescribed N_{it}, the equilibrium step is repeated as described in Section 2.2.

In Fig. 2b the computational steps for solving the semifree boundary value problem are summarized.

5.3. *Mixed Configurations*

Configurations for which the plasma volume is to be controlled (as in Section 5.1) and which resort to more than one coil group (as in Section 5.2) here are called "mixed" configurations. Typical examples are coil setups with a long primary solenoid (e.g., JET) which can be treated as "mixed" or—in a limiting case—as "closed." The solenoid's current is determined by the flux swing requirements necessary to induce and to maintain the plasma current, and not by equilibrium

considerations. If this current is small, as in the initial stages of the discharge, the configuration is "mixed" and the plasma volume is to be controlled (in solving the semifree boundary value problem); the outer plasma boundary is to be adjusted by means of the other coil groups using the same methods as in Section 5.2. Specifically, an elongation of the JET plasma is achieved by the current in coil g_3 which must be positive (i.e., parallel to the plasma current). In fact, the number of turns in this coil available for plasma shaping is reported to be negative ($n_3 = -20$) [7]. The closed configuration can be understood as the limit of the "mixed" configuration, in which the "private flux" of the primary solenoid and the flux generated by coil 1 are sufficient to elongate the plasma (Fig. 9, which is discussed in Section 10 in more detail, gives an example). In this case the current in coil g_3 is small and is only needed to meet the prescribed plasma boundary exactly. The current in the primary solenoid is in this limit determined by the considerations of Section 5.2. Thus the equilibrium belongs to that timepoint in the evolution of the discharge at which the just-computed current agrees with that resulting from the flux swing requirements.

6. Free Boundary Value Problem Resorting to the Driving Voltages

The main difference between the semifree and the free boundary value problem is that in the latter case the circuit equations are employed to predict and correct the coil currents. These equations are

$$V_i = R_i J_{c_i} + L_i \frac{dI_{ci}}{dt} + I_{ci} \frac{dL_i}{dt} + \sum_{\substack{j=1 \\ j \neq i}}^{N_G+1} \left[P_{ij} \frac{dI_{cj}}{dt} + I_{cj} \frac{dP_{ij}}{dt} \right] + \dot{\psi}_{\mathrm{Fe}}, \tag{6.1}$$

$i = 1, 2, ..., N_G + 1$. R_i are the resistances of the coils, V_i the voltages, L_i the self inductances, and $P_{i,j}$ the mutual inductances. Equation (6.1) also comprises the plasma ($j = N_G + 1$). The system (6.1) is to be added to the plasma evolution equations (8.1)–(8.3) and (8.20) in Section 8.

The changes of the flux function due to the iron core Ψ_{Fe} can be accounted for during the corrector steps (Figs. 4). The time step is in general limited by the time scale of the driving voltages, which change rapidly in the case of fast feedback.

We note that the application of Eq. (6.1) provides the possibility of accounting for passive conductors ($V_j = 0$), as e.g., a vacuum vessel without a break. If the solution for the semifree boundary value problem furnishes the coil currents I_{c_j}, the necessary voltages can be computed from Eq. (6.1). This applies also for the primary solenoid, the current of which is mainly determined by the flux swing requirements. However, the currents in the passive conductors cannot be accounted for by solving the semifree boundary value problem.

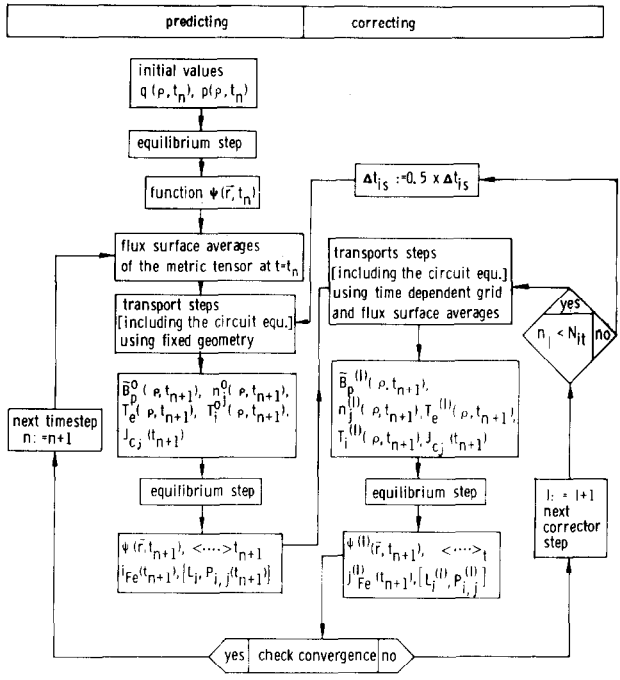

FIG. 4. Iterative method for computing the evolution of a plasma with fixed, semifree, and free boundary. In a first step the method predicts an equilibrium resorting to transport code calculations, which employ a fixed flux surface geometry. During correction in a second step, a time dependent flux surface geometry is used for the transport steps. The noniterative version resorts to the predictor steps only, thus yielding a stepwise evolution of the equilibrium only. The timesteps between the equilibrium calls must be small to ensure that the changes due to the calls of the equilibrium solver are small. Within the square brackets the additional computational steps in case of the free bounary value problem are indicated. The circuit equations need the inductivity matrix P_{ij} ($L_i = P_{ii}$) and the driving voltages as input and are to be solved in addition to the plasma evolution equation.

7. MAGNETIZATION OF THE IRON CORE AND THE YOKES

Especially in open configurations an iron core and yokes are employed to increase and to guide the magnetic flux generated by the OH-coils. Due to the high permeability μ, the iron core and the yokes distort the vacuum magnetic field configuration considerably. The main effect is that the magnetic field lines are almost perpendicular to the surface of the iron if the relative permeability μ_r is sufficiently large. Replacing the yokes and the core by a two-dimensional configuration ("window," Fig. 3) in which the yokes are smeared out toroidally, so that the plasma is surrounded by an iron torus, the magnetic field configuration was computed already by applying a Poisson solver [28]. As the yokes cover a small fraction of the outer circumference of this torus a reduced averaged permeability is

to be introduced. Otherwise the impact of the yokes on the magnetic field configuration might be strongly overestimated.

In the case of simple two-dimensional configurations with $\mu = \infty$ a rough estimate of the iron's action can be obtained by introducing image currents in the domain of the iron modifying the vacuum field so that field lines are perpendicular to the iron surface [29].

Instead of using discrete currents, in this paper the iron core is replaced by an equivalent surface current density changing the magnetic field in the same way as the core, if constant permeability can be assumed approximately in a first step. In the next step a permeability depending on the magnetic field can be assumed as well. The purpose of the yokes is to prevent the demagnetizing field generated by "free magnetic charges" [30] which occur at the ends of the iron core, if this core is used without yokes, and thus to guide the magnetic flux from one end of the core to the other without releasing it to the volume inside the window ("stray field"). To account for this, two options are foreseen:

1. The iron core, replaced by a cylindrical current density, is assumed to be longer than in reality by around a factor 2 so that the flux emanating from its ends hardly affects the magnetic field inside the volume defined by the window. The remaining stray field decreases the field of the coils so that the coil currents might be overestimated.

2. To prevent the stray field, the iron core is complemented by (smeared out)

transitions between the limbs of the yokes and between the iron core and the upper and lower limbs were assumed. These transitions are described by elliptical arcs with the half-axes a_{Fe_j} and b_{Fe_j} $(j = 1, ..., 4)$ (Fig. 3).

A realistic estimate of the image current density standing for the magnetization of the yokes can be achieved by introducing a reduced average (effective) permeability for the yokes so that the magnetic resistance [30] of the smeared out yokes is the same as that of the real yokes and the corresponding air region. The effective permeability is

$$\mu_{\text{eff}} = (N_y \mu_r b_y + 2\pi R - N_y b_y)/2\pi R.$$

N_y is the number of the yokes, b_y their dimension perpendicular to the plane of the cross section in Fig. 3, and R the radial coordinate of Fig. 1. The 2nd treatment describes the saturation of the yokes, which might be important in case of JET.

Two cases, $\mu_r = \infty$ and $\mu_r < \infty$, are envisaged here. The equations for the equivalent surface current densities are given for the iron core only; a generalization to the total window is straightforward.

1. $\mu_r = \infty$

The field lines are perpendicular to the surface of the iron core, i.e., the tangential component of the magnetic induction, B_{tg} vanishes. This condition can be fulfilled

by assuming an axisymmetric current density j_{Fe} in the cylindrical surface. From $B_{tg}=0$ follows a Fredholm equation of the 1st kind for j_{Fe}

$$\int j_{Fe}(z')\frac{\mu_0}{\pi}D(R_F, z; R'_f, z')\,dz' = -B_{\mathrm{pl}}(R_F, z) - B_{\mathrm{c}}(R_F, z). \tag{7.1}$$

The tangential components of the magnetic inductions due to the plasma current and the coil currents, B_{pl} and B_{c}, respectively, are

$$B_{\mathrm{pl}}(R_F, z) = \int j_t(R_p, z_p)\frac{\mu_0}{\pi}D(R_F, z; R_p, z_p)\,dR_p\,dz_p \tag{7.2}$$

and

$$B_{\mathrm{c}}(R_F, z) = \sum J_{cj}\frac{\mu_0}{\pi}D(R_F, z; R_{cj}, z_{cj}). \tag{7.3}$$

The coordinates (R_F, Z) and (R'_F, Z') denote the test and the source points. R'_F is the radius of the core (Fig. 3). R_F is slightly larger than R'_F; the difference $R_F - R'_F$ is given at the end of the section. The source points of the plasma and the coils are (R_p, Z_p) and (R_{cj}, Z_{cj}), respectively. The quantity

$$D(R, z; R', z') = \frac{k}{4\sqrt{RR'}}\left[K(k) + \frac{R'^2 - R^2 - (z-z')^2}{(R-R')^2 + (z-z')^2}E(k)\right]. \tag{7.4}$$

is essentialy the vertical (z)-component of the magnetic field generated at (R, z) by a circular conductor with radius R' and height z'.

2. $\mu_r < \infty$

In this case the discontinuity relation for the tangential component of the magnetic induction is employed, written in terms of the continuous tangential component of the magnetic field H_{tg}

$$B_{1_{\mathrm{tg}}} - B_{2_{\mathrm{tg}}} = \mu_0(\mu_r - 1)H_{\mathrm{tg}}. \tag{7.5}$$

[redacted]

Ampere's law on the infinitesimal small volume indicated in Fig. 3, one gets the relation

$$B_{1_{\mathrm{tg}}} - B_{2_{\mathrm{tg}}} = \mu_0 j_{\mathrm{Fe}}. \tag{7.6}$$

It follows, e.g., from Biot–Savart's law, that at the surface of the core $j_{\mathrm{Fe}}(z)$ generates a tangential component only so that the normal component of the induction B_n is not affected. Hence the continuity relation

$$B_{n_1} = B_{n_2}$$

holds as well. From (7.6) and (7.5) we get a Fredholm equation of the 2nd kind

$$\mu_0 j_{\mathrm{Fe}}(R_F, z) = \mu_0(\mu_r - 1) \int j_{\mathrm{Fe}}(R_F, z') \frac{1}{\pi} D(R_F, z; R'_F, z')\, dz' + (\mu_r - 1)(B_{\mathrm{pl}}(R_F, z) + B_{\mathrm{c}}(R_F, z')). \tag{7.7}$$

For $\mu_r = 1$ (saturated iron) we have $j_{\mathrm{Fe}}(z) = 0$. If $\mu_r \gg 1$, Eq. (7.1) is obtained.

Gauss-integration with up to $N_{\mathrm{Fe}} = 100$ nodes can be employed to convert the integral equations (7.1) and (7.7) into matrix equations.

To ensure that the field generated by the discretized current density j_{Fe} is sufficiently smooth at the testpoints (R_F, Z), $R_F = R_{F'} + \varepsilon_{\mathrm{Fe}}$ is used, where $\varepsilon_{\mathrm{Fe}}$ is of the order of the distance $d_{\mathrm{Fe}} = W_{\mathrm{Fe}_y}/N_{\mathrm{Fe}} \approx 5$ cm between the current-carrying filaments standing for j_{Fe}. We note that $\varepsilon_{\mathrm{Fe}}$ is small compared to the major radius.

The solution of Eq. (7.7) in configuration space requires an inversion of high rank matrices. This can be avoided in general if the current density j_{Fe} is expanded by using, e.g., (normalized) Legendre polynomials as an orthonormal basis. The thus obtained Legendre representation of Eq. (7.7) is

$$\sum_{j=0}^{N_L} M_{i,j} j_{\mathrm{Fe}_j} = \frac{\mu_0}{\pi} \sum_{j=0}^{N_L} D_{i,j} j_{\mathrm{Fe}_j} + B_{\mathrm{pl}_i} + B_{\mathrm{c}_i}. \tag{7.8}$$

The matrices $D_{i,j}$, $M_{i,j}$ and the vectors B_{pl_i}, B_{c_i}, j_{Fe_i} are given by

$$D_{i,j} = \int_{S_a}^{S_b} \int_{S'_a}^{S'_b} D(S, S')\, P_i(S)\, P_j(S')\, dS\, dS'$$

$$B_{\mathrm{pl}_i} = \int_{S_a}^{S_b} B_{\mathrm{pl}}(S)\, P_i(S)\, dS$$

$$B_{\mathrm{c}_i} = \int_{S_a}^{S_b} B_{\mathrm{c}}(S)\, P_i(S)\, dS$$

$$j_{\mathrm{Fe}_i} = \int_{S_a}^{S_b} j_{\mathrm{Fe}}(S)\, P_i(S)\, dS$$

$$M_{i,j} = \mu_0 \int_{S_a}^{S_b} \frac{P_i(s)\, P_j(s)}{\mu_{\mathrm{eff}} - 1}\, ds.$$

$S = (R_F, Z)$ and $S' = (R'_F, Z')$ are the test and the source points, respectively. S_a and S_b denote the starting and end points of the envisaged interval defined by the core. $P_i(S)$ is the (slightly modified) Legendre polynomial normalized in (S_a, S_b). If the yokes are accounted for, the test points S_{T} is defined by the arc length between the origin 0 and S_{T} (Fig. 3). The calculations show that the results for $N_L \geqslant 30$ are almost insensitive with respect to N_L; therefore $N_L = 30$ is used in Section 10.

As saturation effects are important, during the PDE–ODE iteration the field

dependence of μ_r can be introduced by a backaveraging procedure. We note however, that the solution of (7.7) only describes in the case of constant μ_r, the field penetration into the iron, correctly. Here we concentrate on the field configuration outside the iron. There the field computed by means of j_{Fe} should be a good approximation as the impact of the discontinuity relation (7.5) is in general dominating. This is confirmed by comparison with the TEXTOR results (Section 10).

We note that the matrix $M_{i,j}$ becomes diagonal $M_{i,j}=\delta_{i,j}/(\mu_{\mathrm{eff}}-1))$, if a constant μ_{eff} is assumed. The matrix $D_{i,j}$ depends on the geometry of the transformer iron only and needs to be computed one time only. $M_{i,j}$, however, depends in general via $\mu_r(|\mathbf{B}|)$ on the fields generated by the coils and the plasma current and on the field evoked by j_{Fe}, i.e., the magnetization. By storing the geometry-dependent parts in the expressions for these fields which are analogous to (7.2) the computation of $|\mathbf{B}|$ can be vectorized. The calculation of $B_{\mathrm{pl},i}$, $B_{\mathrm{c},i}$, and $M_{i,j}$ can be vectorized as well, since $P_i(s_k)$ need to be computed initially only and the field components $B_{\mathrm{pl}}(s_k)$ and $B_{\mathrm{c}}(s_k)$ one time at each iteration step; s_k are Gaussian nodes ($k=1, ..., 100$).

8. Time Evolution of the Particle Densities, The Temperatures, and the Magnetic Fields

The time evolution of the electron and ion temperatures depends essentially on the power and distribution of the energy sources, as Ohmic, neutral injection, or high frequency heating, and of the energy losses effected by conduction, convection, line radiation, bremsstrahlung, cyclotron radiation, charge exchange, ionization, and recombination. The particle source and loss mechanisms which determine the particle inventory, are the diffusion perpendicular to the magnetic field, the inward flow, deposition by neutral injection heating, neutralization at the limiter or divertor plate, and the recycling processes.

Accounting for the processes mentioned above and for an evolving flux surface geometry, one arrives at the following transport equations [14–19] for the particle densities n_j and the electron and ion temperatures T_e, T_i of a multispecies plasma

$$\frac{\partial n_j}{\partial t}=-\frac{1}{\rho}\frac{\partial}{\partial\rho}\left[\rho\langle|\nabla\rho|^2\rangle\Gamma_j\right]+S_{A_j}+S_j + S_{ex_j}+S_{hj}+S_{\alpha j}+S'_L\theta(\rho-\rho_p), \tag{8.1}$$

$j=1, ..., 6;$

$$\frac{3}{2}\frac{\partial}{\partial t}(n_e k T_e)=\frac{1}{\rho}\frac{\partial}{\partial\rho}\left[K\rho\langle|\nabla\rho|^2\rangle\left(\chi_e n_e\frac{\partial T_e}{\partial\rho}-\frac{3}{2}T_e\Gamma_e\right)\right]+P_{c_i} + P_{RF_e}+P_{A_e}+P_{\mathrm{eq}}+P_{\mathrm{fl}}+P_{\mathrm{OH}}+P_{b_e} + P_{\alpha_e}+P_{\mathrm{rad}}+P'_{L_e}\theta(\rho-\rho_p); \tag{8.2}$$

$$\frac{3}{2}\frac{\partial}{\partial t}(n_i k T_i) = \frac{1}{\rho}\frac{\partial}{\partial \rho}\left[k\rho\langle|\nabla\rho|^2\rangle\left(\chi_i n_i \frac{\partial T_i}{\partial \rho} - \frac{3}{2} T_i \Gamma_i\right)\right] + P_{c_i}$$
$$+ P_{\mathrm{RF}_i} + P_{A_i} - P_{\mathrm{eq}} - P_{\mathrm{fl}} + P_{b_i}$$
$$+ P_{cx} + P_{\alpha_i} + P'_{L_e}\theta(\rho - \rho_p). \tag{8.3}$$

These equations are solved by means of the plasma module, the flow chart of which is depicted in Fig. 5, which shows the interaction with the other modules as well. The flux density Γ_j of ion species j, the equilibration term P_{eq}, the effective mass m_{eff}, the analogous effective charge number Z_{eff}, the flow work P_{fl}, the total ion convection flux Γ_i, and the electron convection flux Γ_e are

$$\Gamma_j = -D_j \frac{\partial n_j}{\partial \rho} - \frac{2D_j \rho}{\rho_p^2} n_j + \Gamma_{nj} \tag{8.4}$$

$$P_{\mathrm{eq}} = \frac{3m_e}{m_{\mathrm{eff}}} \frac{n_e}{T_e}(T_i - T_e) \tag{8.5}$$

$$\frac{1}{m_{\mathrm{eff}}} = \frac{\sum_{j=1}^{6} n_j \langle z_j^2\rangle / m_j}{\sum_{j=1}^{6} n_j}$$
$$z_{\mathrm{eff}} = \left(\sum_{j=1}^{6} \langle z_i^2\rangle n_j\right) \Big/ n_e \tag{8.6}$$

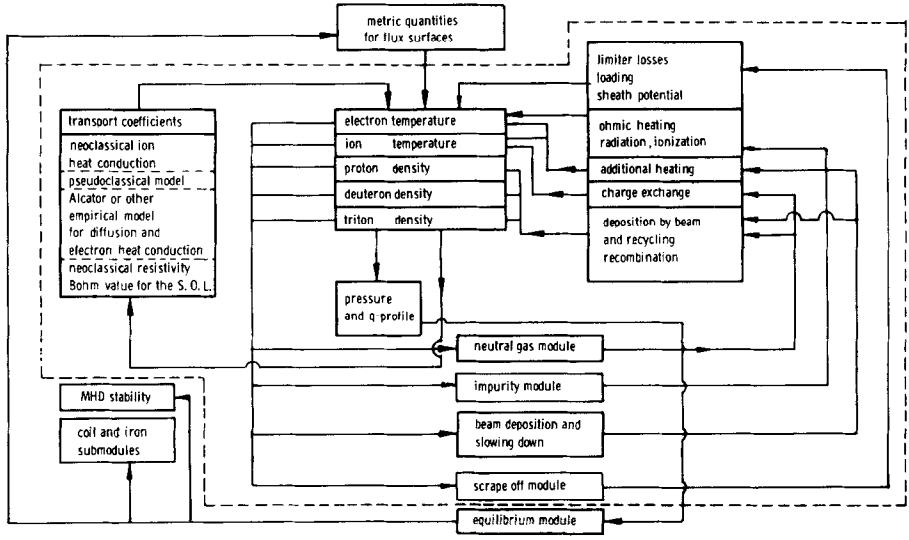

FIG. 5. Flow chart of the 1 ½ D-code TORUS II; within the broken line the chart of the 1D-code TORUS I is given. The transport equations account for the source terms provided by the neutral gas, the impurity, the beam deposition, the slowing down, and the scrape-off modules. The equilibrium module provides 2D-flux surface geometry, the metric quantities, the outer magnetic fields, and some stability information.

$$P_{\text{fl}} = \frac{\Gamma_e}{n_e} \frac{d}{d\rho} (n_i T_i) \tag{8.7}$$

$$\Gamma_i = \sum_{j=1}^{6} \Gamma_j \tag{8.8}$$

$$\Gamma_e = \sum_{j=1}^{6} \langle z_j \rangle \Gamma_j; \tag{8.9}$$

$j = 1$ stands for the protons,

$j = 2$ for the deuterons,

$j = 3$ for the tritons,

$j = 4$ for the α particles,

$j = 5$ for a light impurity species (carbon or oxygen),

$j = 6$ for a heavy impurity species (iron or molybdenum),

$\langle |\nabla \rho|^2 \rangle$ is the metric quantity accounting for the shape of the flux surface [3],

k is Boltzmann's constant,

D_j the diffusion coefficient of the ion species j,

χ_e the electron heat diffusivity,

χ_i the ion heat diffusivity,

m_j the mass of the ion species,

m_{eff} the effective mass,

$\langle Z \rangle_f$ the average charge number of the species j, and

$\langle Z^2 \rangle_j$ the average squared charge number. For the hydrogen species the convention $\langle Z_1 \rangle = \langle Z_2 \rangle = \langle Z_3 \rangle = \langle Z_1^2 \rangle = \langle Z_2^2 \rangle = \langle Z_3^2 \rangle = 1$ is used;

$$n_e = \sum_{i=1}^{6} \langle z_j \rangle n_j$$

and

$$n_i = \sum_{j=1}^{6} n_j$$

are the total electron and ion density, respectively. The impurity quantities, n_j and Γ_j, are sums over all ionization stages; the average ion model is adopted throughout [39] and sputtering is assumed as impurity source [40].

The sink terms S_j', P_e', P_i' are switched on in $\rho_p < \rho < \rho_w$ by the Heaviside step function $\theta(\rho - \rho_p)$ if the devices defining the plasma aperture are accounted for explicitly. In this paper only limiters are envisaged [47–50]. ρ_w defines, together

with ρ_p, the extension of the scrape-off layer. The boundary conditions at $\rho = \rho_w$ are pedestal conditions; they are

$$T_e(\rho_w) = T_i(\rho_w) = 5\ \text{eV}$$
$$n_j(\rho_w) = 0.05 \times n_j(\rho = 0)|_{t=0},$$
$$j = 1, ..., 6.$$

The scrape-off layer is not included in the equilibrium calculations. The metric quantities computed at $\rho = \rho_p$ are used in $\rho_p < \rho < \rho_w$ as well.

For many questions concerning the core plasma radial resolution in the scrape-off layer is not important and the limiters are roughly accounted for by the boundary conditions at $\rho = \rho_p$ only. These are

$$T_e(\rho_p) = T_i(\rho_p) = 25\ \text{eV}$$
$$n(\rho_p) = 0.1\ n_j(\rho = 0)|_{t=0}$$
$$j = 1, ..., 6.$$

The energy source and sink term P_{OH}, $P_{\alpha_{e,i}}$, $P_{b_{e,i}}$, $P_{\text{RF}_{e,i}}$, P_{rad}, P_{cx}, $P_{C_{e,i}}$; P_{eq}, P_{fl} stand for Ohmic, α-particle, beam- and *RF*-heating [42–44], radiation, charge exchange, temperature control [45–46], equilibriation, and for the flow-work of the ions [1] transferred to the electrons, respectively. Specifically, the ohmic heating term [13] is given by

$$P_{\text{OH}} = \langle jE \rangle_\rho = \eta_{//} \frac{f}{A} \frac{1}{\rho} \frac{\partial}{\partial \rho} \left(\rho \left\langle \frac{|\nabla \rho|^2}{R^2} \right\rangle \frac{\tilde{B}_p}{f} \right)$$
$$\times \frac{1}{\rho} \frac{\partial}{\partial \rho} \left(\left\langle \frac{|\nabla \rho|^2}{R^2} \right\rangle \rho \frac{\tilde{B}_p}{f} \right). \tag{8.10}$$

(8.10) accounts for the fact that neither the current density j nor the electric field E are surface quantities. The quantities f, A, R, $\tilde{B}_p$ and the average value $\langle |\nabla \rho|^2 / R^2 \rangle$ are defined in Section 2. The neoclassical expression for the parallel resistivity $\eta_{//}$ in Ref. [1] is employed; however, the radial coordinate there is replaced here by the effective radius ρ and the effective charge number (8.7) is introduced. We note that the (generalized) radiation losses (P_{rad}) comprise the ionization (P_{io_I}), line radiation (P_{lin_I}), and bremsstrahlung losses (P_{br_I}) evoked by the impurity species [41] and the hydrogen ionization and bremsstrahlung losses, P_{io_H} and P_{br_H}, i.e., P_{rad} is

$$P_{\text{rad}} = P_{\text{io}_I} + P_{\text{lin}_I} + P_{\text{br}_I} + P_{\text{io}_H} + P_{\text{br}_H}.$$

The hydrogen line radiation losses are neglected. The particle source terms S_j, S_{cx_j}, S_{b_j}, and S_{α_j} account for the ionization of the neutral particles [20–23], for the (nondiagonal) charge exchange reactions, for neutral injection, and for fusion. The

source terms S_{A_j}, P_{A_e} and P_{A_i} account for the adiabatic changes of the plasma parameters due to the evolution of the flux surface geometry; they are given by

$$S_{A_j} = -n_j \frac{1}{\dot{V}} \frac{\partial \dot{V}}{\partial t} \tag{8.11}$$

$$P_{A_e} = -nkT_e \frac{1}{\dot{V}^\gamma} \frac{\partial \dot{V}^\gamma}{\partial t} \tag{8.12}$$

$$P_{A_i} = -nkT_i \frac{1}{\dot{V}^\gamma} \frac{\partial \dot{V}^\gamma}{\partial t}. \tag{8.13}$$

The dot denotes the derivative with respect to ψ; $\gamma = \frac{5}{3}$ is the adiabatic constant.

In Fig. 4 the iteration scheme is shown for the computation of the equilibrium evolution. The calculation is started ($t = t_0 = 0$) with a consistent set of plasma and magnetic field parameters.

During the predictor step a fixed flux surface geometry is used in order to estimate the equilibrium quantities at $t = t_1$. In correcting, a variable geometry can be employed by interpolating between the quantities at $t = t_0$ and the predicted (or corrected for $l \geqslant 1$) quantities at $t = t_1$. In Fig. 4 the index 0 is replaced by n and the index 1 by $n+1$ because the same considerations are valid for an arbitrary timestep. The iteration is stopped if the maximum of

$$d_1 = \sup \frac{|q_l(\Psi) - q_{l+1}(\Psi)|}{q_l(\Psi)}$$

and

$$d_2 = \sup \frac{|p_l(\Psi) - p_{l+1}(\Psi)}{p_l(\Psi)}$$

becomes smaller than a prescribed accuracy parameter ε_3. A simplified (non-iterative) computational scheme resorts essentially to the predictor step of Fig. 4. In this case the source terms (8.11)–(8.13) are not used; the adiabatic transformations

$$\hat{T}_e(\Psi) = \frac{\dot{V}^{\gamma-1}}{\hat{\dot{V}}^{\gamma-1}} T_e(\psi) \tag{8.14}$$

$$T_i(\Psi) = \frac{\dot{V}^{\gamma-1}}{\hat{\dot{V}}^{\gamma-1}} T_i(\Psi) \tag{8.15}$$

$$\hat{n}_j(\Psi) = \frac{\dot{V}}{\hat{\dot{V}}} n_j(\Psi), \qquad j = 1, 2, ..., 6, \tag{8.16}$$

are employed instead after each equilibrium step.

The applicability of the simplified scheme must in principle be checked by

the iterative scheme. However, if the flux surface geometry changes slowly it can be expected that the simplified schemes describes the discharge in a good approximation.

A simple empirical model is chosen [3] for the transport coefficients D and χ_e; χ_i is obtained from neoclassical theory [1]:

$$D/\chi_e = 0.25 \tag{8.17}$$

$$\chi_e = \frac{5 \cdot 10^{17}}{n_e \,\mathrm{cm}^3} \frac{\mathrm{cm}^2}{\mathrm{s}} \tag{8.18}$$

$$\chi_i = f(\nu_i^*)\, q^2 \rho_i^2 \nu_{ii}. \tag{8.19}$$

The function $f(\nu_i^*)$, depending on the collisionality ν_i^*, is given in [1]. q is the safety factor, ρ_i the ion Larmor radius and ν_{ii} the ion-ion collision frequency. Instead of the neoclassical inward flow term ("Ware pinch") [1, 3], the phenomenological inward flow term advanced by Engelhardt *et al.* [31] is used in Eq. (8.4). The neoclassical fluxes Γ_{nj} are neglected in the case of the hydrogen species ($j = 1, 2, 3$) but taken into account in the case of the impurity species ($j = 4$, 5, 6) [39]. This rough procedure is probably justified as in practice nonclassical processes dominate the transport. The evolution equations (8.1)–(8.3) are completed by equations for either the poloidal or the toroidal flux function given in [6] and written here in terms of ρ and the effective poloidal and toroidal magnetic inductions $\tilde{B}_p$ and $\tilde{B}_t$ both defined in Section 2,

$$\frac{\partial \tilde{B}_p}{\partial t} = \frac{1}{\mu_0} \frac{\partial}{\partial \rho} \left[\eta_{\shortparallel} \frac{f}{A} \frac{1}{\rho} \frac{\partial}{\partial \rho} \left(\rho \left\langle \frac{|\nabla \rho|^2}{R^2} \right\rangle \frac{\tilde{B}_p}{f} \right) \right] + S_{B_p} \tag{8.20}$$

$$\frac{\partial \tilde{B}_t}{\partial t} = \frac{1}{\mu_0} \frac{1}{\rho} \frac{\partial}{\partial \rho} \left[\eta_{\shortparallel} \rho \left\langle \frac{|\nabla \rho|^2}{R^2} \right\rangle \frac{\partial}{\partial \rho} \left(\frac{\tilde{B}_t}{A} \right) \right] + S_{B_t}. \tag{8.21}$$

The source term S_{B_p} and S_{B_t} read

$$S_{B_p} = -\frac{1}{R_0} \frac{\partial}{\partial \rho} \left(\frac{\dot{\chi}}{q} \right) \tag{8.22}$$

and

$$S_{B_t} = \frac{1}{\rho} \frac{\partial}{\partial \rho} q \left(\dot{\psi} - \frac{R_0 \eta_{\shortparallel}}{A \mu_0} \frac{1}{\rho} \frac{\partial}{\partial \rho} \left(\rho \left\langle \frac{|\nabla \rho|^2}{R^2} \right\rangle \tilde{B}_p \right) \right). \tag{8.23}$$

The equivalent equations (8.20) and (8.21) describe the magnetic field diffusion. A similar procedure as in case of Eq. (8.1)–(8.3) accounts for the movement of the flux surfaces.

The time-centered source terms S_{B_p} or S_{B_t} computed by an interpolation can be obtained by the iterative version only. In the case of the noniterative scheme,

only an extrapolation based on the last two equilibrium calls can be used. This presupposes that the time-dependence of the source terms is weak.

Equation (8.20) is to be chosen if the changes of the toroidal field are small and the changes of the poloidal field are dominant. Examples are the current rise and the flat top phase during normal Tokamak operation because changes of the currents in the toroidal field coils are in general difficult to achieve by engineering reasons already. In the case of the TUMAN compression experiment [32], Eq. (8.21) describes the penetration of the toroidal field after the compression phase. Here only normal Tokamak operation is investigated and therefore Eq. (8.20) is used throughout. Finally, we note that among the possible evolution equations [6], (8.20) and (8.21) were chosen to allow the transition to the familiar poloidal and toroidal field diffusion equations [33] in a straightforward way.

Between the timepoints t_n and t_{n+1} (Fig. 4), several transport step Δt_p are inserted during which the coupled system (8.1)–(8.3) and (8.20) (or 8.21) are solved iteratively at certain timepoints t_m ($t_n < t_m < t_{n+1}$). A predictor-corrector method is used analogously to that described in Ref. [23] for a system of coupled diffusion equations. The Crank–Nicholson differencing, the accuracy prescription for the correcting and the timestep control described there are used here as well.

The equidistant grids (ρ_j) and $(\rho_{i+1/2})$ are rescaled before each timestep Δt_p according to the evolution of the plasma volume V_p, thus accounting for one part of the movement of the flux surfaces. This movement occurs even in the case of the fixed boundary value problem because of the finite accuracy in the computation of the plasma boundary. The (possibly less important) movement of the flux surfaces relative to the grid (ρ_j) is accounted for by employing an auxiliary grid $\{\bar{\rho}(\psi_j)\}$ synchronized with the flux surfaces exactly and transforming the plasma parameters from the $\{\bar{\rho}(\psi_j)\}$ grid to the $\{\rho_j\}$ grid after each timestep.

Also the equilibrium quantities as $\langle |\nabla\rho|^2 \rangle$ are calculated by an interpolation before each timestep Δt_p presupposing that the variation of these quantities can be approximated linearly between two equilibrium calls.

A flowchart of the one-dimensional transport code, together with the codes for the neutral gas background, the impurities, additional heating, and the scrape-off layer, is shown within the broken line of Fig. 5 ("TORUS I"); outside the broken line the two-dimensional equilibrium code and its submodules are displayed which allow in conjunction with TORUS I the "1 $\frac{1}{2}$ D" description ("TORUS I").

We note that the computation of the tridiagonal matrices which are to be inverted in solving the system (8.1)–(8.3) and (8.20) is vectorized essentially by storing some of the source terms and their derivatives with respect to the plasma parameters at each predictor and the coefficients at each corrector-predictor step. The majority of the source terms, e.g., those evoked by additional heating and the neutral gas are computed at selected time points and assumed to be constant in the time intervals between the calls.

During the evolution of the discharge the Mercier criterion and Glasser criterion for the ideal and the resistive interchange MHD stability, respectively, may be checked [3, 38]. They require $D_I < 0$ and $D_R < 0$, where the quantities D_I and D_R

account, e.g., for the destabilizing effect of the pressure gradient are given in [3, 51]. However, the just mentioned conditions do not exclude the onset of MHD activity completely which might distort or destroy the flux surface geometry by ideal or resistive modes. These modes possibly evoke another transport behaviour than described by (8.18) or even terminate the discharge [52–58]. Therefore β-, density, and safety factor limits are checked also [59–62].

9. Particle Flux and Power Balances

Integrating equations (8.1), (8.2), and (8.3) over the plasma volume in $0 < \rho < \rho_p$ yields the rate of change of the particle and energy inventory

$$\dot{N}_j = \bar{S}_{\mathrm{D}j} + \bar{S}_A + \bar{S}_j + \bar{S}_{cxj} + \bar{S}_{bj} + \bar{S}_{\alpha j} \tag{9.1}$$

$$\dot{E}_e = \bar{P}_{\mathrm{CD}_e} + \bar{P}_{\mathrm{CV}_e} + \bar{P}_{A_e} + \bar{P}_{\mathrm{eq}} + \bar{P}_{\mathrm{fl}} + \bar{P}_{\mathrm{OH}} + \bar{P}_{C_e} + \bar{P}_{b_e} + \bar{P}_{\alpha_e} + \bar{P}_{\mathrm{RF}_e} + \bar{P}_{\mathrm{io}_H} + \bar{P}_{\mathrm{rad}_l} + \bar{P}_{\mathrm{br}_H} \tag{9.2}$$

$$\dot{E}_i = \bar{P}_{\mathrm{CD}_i} + \bar{P}_{\mathrm{CV}_i} + \bar{P}_{A_i} - \bar{P}_{\mathrm{eq}} - \bar{P}_{\mathrm{fl}} + \bar{P}_{\mathrm{RF}_i} + \bar{P}_{b_i} + \bar{P}_{C_i} + \bar{P}_{CX} + \bar{P}_{\alpha_i}. \tag{9.3}$$

$\bar{S}_{D_j}$, $\bar{P}_{\mathrm{CD}_{e,i}}$, and $\bar{P}_{\mathrm{CV}_{e,i}}$ stand for the diffusive particle losses, the conductive and the convective energy losses. $\bar{P}_{\mathrm{rad}_l}$ comprises the impurity radiation losses, i.e., $\bar{P}_{\mathrm{rad}_l} = \bar{P}_{\mathrm{lin}_l} + \bar{P}_{\mathrm{br}_l} + \bar{P}_{\mathrm{io}_l}$. The remaining quantities, as $\bar{S}_A$, $\bar{S}_j$, etc. (always marked by bars), are obtained from the corresponding quantities in Eq. (9.1)–(9.3) by a volume integration. Time integration of Eq. (9.1)–(9.3) yields

$$N_j = N_j(t=0) + \int_0^t \dot{N}_j(\tau)\, d\tau \tag{9.4}$$

and analogous equations for E_e and E_i. The LHS of Eq. (9.1) and (9.4) can be computed from the spatial and temporal evolution of the particle densities $n_j(r)$ as well, resulting in $\bar{\dot{N}}_j$ and $\bar{N}_j$. Analogous considerations hold for the energy contents E_e and E_i, yielding $\bar{\dot{E}}_e$, $\bar{E}_e$, $\bar{\dot{E}}_i$, and $\bar{E}_i$. The relative deviations

$$\frac{|\dot{N}_j - \bar{\dot{N}}_j|}{\mathrm{Max}(s)}, \quad \frac{|\dot{E}_i - \bar{\dot{E}}_i|}{\mathrm{Max}(P_i)}, \quad \frac{|\dot{E}_e - \bar{\dot{E}}_e|}{\mathrm{Max}(P_e)}, \quad \frac{|\bar{N}_j(t) - N_j(t)|}{N_j(t)},$$

$$\frac{|E_i(t) - \bar{E}_i(t)|}{E_i(t)} \quad \text{and} \quad \frac{|E_e(t) - \bar{E}_e(t)|}{E_e(t)}$$

stay below $\delta_1, \delta_2, \ldots, \delta_6$, respectively, in all calculations mentioned in Section 10; δ_j ($j = 1, 2, \ldots, 6$) are given by $\delta_1 = 10^{-3}$, $\delta_2 = \delta_3 = 5 \cdot 10^{-3}$, $\delta_4 = 10^{-2}$, $\delta_5 = \delta_6 = 5 \cdot 10^{-2}$. Max($S$), Max($P_e$), and Max($P_i$) denote the maxima of the absolute values of the terms on the RHS of Eq. (9.1)–(9.3).

10. Results

In this section a medium-size device, TEXTOR with circular plasma, a major device, JET, with an elongated plasma, and a reactor–like Tokamak, INTOR, are envisaged. The first two devices allow a comparison with experimental data. However, it is mainly intended to demonstrate the numerical feasibility and consistency of the code rather than a detailed comparison with these data or a thorough transport analysis; the reason is that the simple empirical transport model cannot be expected to describe the particle and energy inventory with high accuracy. Therefore the results preferentially concern the magnetic field structure generated by the plasma, the coils, and the iron. In fact, the Grad–Shafranov equation provides a more reliable basis for the pressure balance than the transport equations do for, e.g., the electron energy balance.

For the computations an IBM 3033 V/2 computer interacting with an MVS (multiple virtual storage) batch system and a CRAY X-MP computer interacting with a COS 1.12 (CRAY-operating) batch system were employed.

In the case of the semifree boundary value problem, solved for TEXTOR (open configuration) and JET (closed configuration), the noniterative version of Fig. 4 was used because the maximum possible timestep between the equilibrium calls was chosen to be small (30 ms for TEXTOR and 50 ms for JET) and the equilibrium

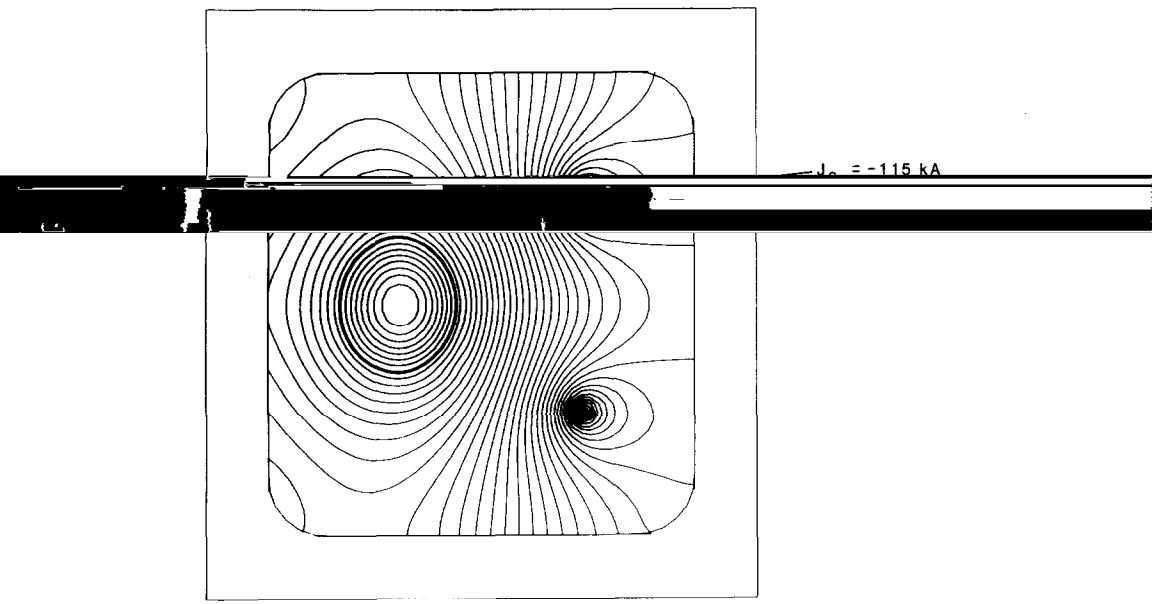

Fig. 6. Flux function inside and outside the TEXTOR plasma with iron core and yokes which are accounted for by Eq. (7.8) employing a representation by trigonometric functions; μ_{eff} is geometry and field dependent.

evolves slowly. Other reasons are the rather large CPU-times for the coil and the iron module. In the case of INTOR for which the fixed boundary value problem was solved the iterative and the noniterative versions were employed. A comparison revealed no significant changes, except for the fact that in the iterative version the time evolution of the particle and energy contents and of the corresponding fluxes becomes continuous because the geometry of the flux surfaces changes continuously as well; the accuracy parameter was $\varepsilon_3 = 3\%$.

10.1. *TEXTOR*

The main TEXTOR data are [28]: plasma radius $\rho_p = 50$ cm, major radius $R_0 = 175$ cm, plasma current $I_p = 476$ kA, vacuum value of the toroidal field (at $R = R_0$), $B_{t0} = 20$ kG. The coil and the transformer iron data are indicated in Fig. 6. This figure displays mainly the flux function inside the window.

The iron core and the yokes were accounted for by means of the representation (7.8) employing trigonometric functions as the orthonormal basis. A geometry and field-dependent permeability was assumed.

Almost the same result as in Fig. 6 is obtained if Legendre polynomials or Chebyshev polynomials of the first kind are used. This confirms that the results are appoximately independent from the basis. Because of the toroidicity [33] and the attraction by the yokes the cross section in Fig. 6 is somewhat elongated. This

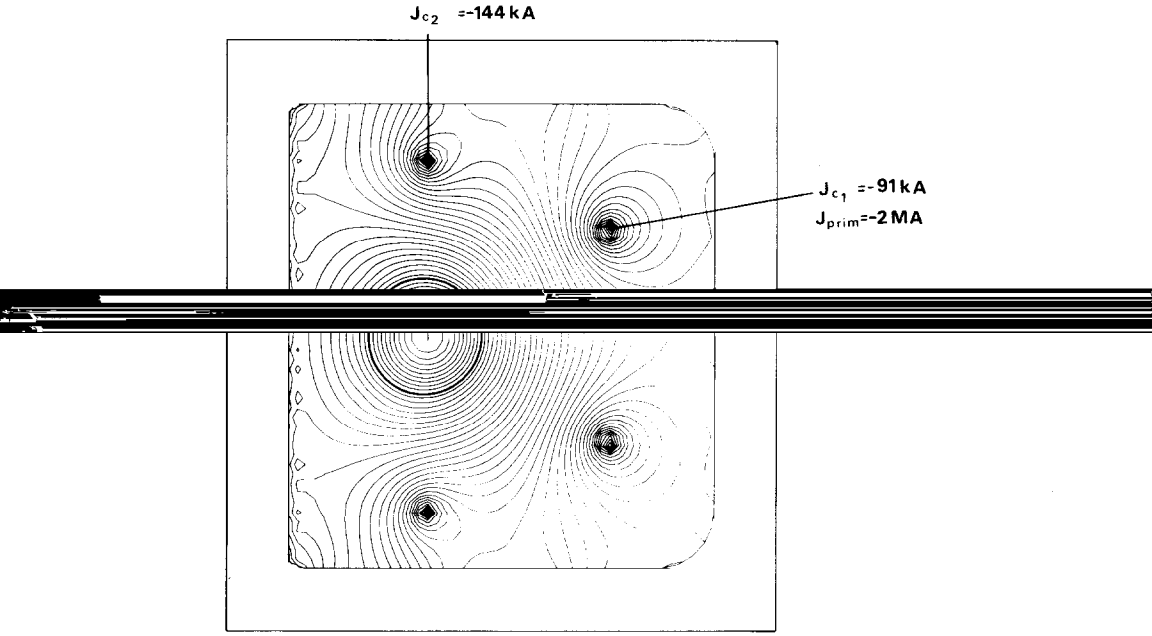

FIG. 7. Mixed configuration with a primary solenoid and two shaping coils. The current in the primary solenoid I_{prim} is prescribed. I_{c_1} and I_{c_2} are adjusted to shape and position the plasma.

elongation disappears if the OH-coils of Fig. 3 are taken into account. The reasons are the reduced permeability in the vicinity of the coils and their shaping effect. The circular cross section is corroborated experimentally. To provide a better guidance for the OH-flux and thus to enhance the flux swing, the OH-coils in Fig. 7 are replaced by a long primary solenoid with prescribed current $I_{\text{prim}} = 2$ MA and two shaping coils top and bottom of the plasma are added to maintain the circular cross section. This setup is an example of a mixed configuration (Section 5.3). The current I_{c_1} is smaller than the analogous current in Fig. 6. because the current in the shaping coils contribute to the vertical field as well.

In Fig. 8 the time evolution of the coil current centering the plasma between two rail limiters at $x = \pm \rho_L$ is given: without iron core (a), with iron core and assuming $\mu = \infty$ (b), with iron core and employing a field-dependent permeability (c). Curve (d) stands for the the experimental dependence. Only in case (c) is the maximum deviation from the experimental curve small (8%). This stresses the importance of the transformer iron for the force balance. The plasma parameters emanating from a programmed gas feed and ohmic heating may, during the flat top phase, be characterized by the maximum values $n_{i_{\max}} = 3.7 \times 10^{13}/\text{cm}^3$, $T_{e_{\max}} = 790$ eV, $T_{i_{\max}} = 740$ eV, $Z_{\text{eff}_{\max}} = 1.5$ for the proton density, electron and ion temperatures, and the effective charnge number, respectively.

10.2. *JET*

The calculations are based on two data sets: the first concerns a scenario with powerful additional heating which will be available in future JET shots [35, 36]. The second concerns shot 6296 with ohmic heating only [37].

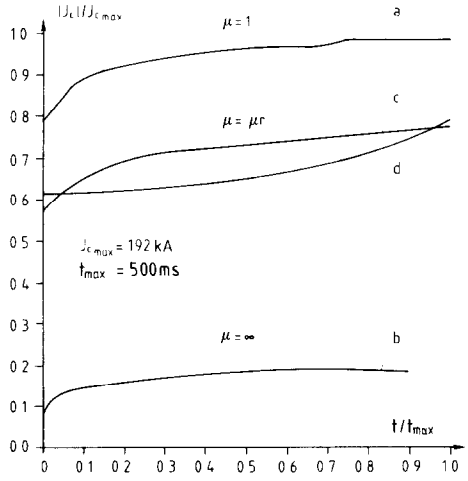

Fig. 8. Time evolution of the poloidal field coil currents in TEXTOR without (a), with iron core and $\mu = \infty$ (b), and with iron and $\mu = \mu(|\mathbf{B}|)$ (c); curve (d) shows the experimental evolution dependence (shot 5465).

In the first case the JET data are $\rho_p = 165$ cm, $R_0 = 297$ cm, ellipticity $\varepsilon = 1.77$, excentricity $e = 1.66$, D-shape $d = 1.2$, toroidal field $B_{t_0} = 35$ kG, plasma current $J_p = 4.80$ MA. The data for additional heating, neutral injection (NI), and ion cyclotron resonance heating (ICRH) are: beam turn-on time $t_{B_1} = 0$, beam turn-off time $t_{B_2} = 5$ s, beam power $P_B = 17.25$ MW, and beam energy $E_B = 160$ keV. The injected species is deuterium and co-injection is assumed. A full-beam geometry is used. The main geometrical data of the beamline are [36]: Portwidth $a_w = 33$ cm, portheight $a_h = 77.6$ cm horizontal focal length $f_h = 1000$ cm, vertical focal length $f_v = 1400$ cm, horizontal divergence $d_h = 0.7°$, vertical divergence $d_v = 0.7°$, and the angle between the beam axis and the straight line connecting the pivot point with the torus center $\alpha_3 = 16.34°$.

The ICRH power is $P_{RF} = 20$ MW, the ICRH turn-on time $t_{I_1} = 1$ s, and the ICRH turn-off time $t_{I_2} = 5$ s. A density-weighted deposition profile was assumed. The geometry of the coils, the iron core, and the yokes [7] is displayed in Fig. 9. By the choice of $a_{Fe_i} = 1.40$ m and $b_{Fe_i} = 1.40$ m $(i = 1, ..., 4)$ it is attempted to account for the fact that the iron core has a larger diameter at the top and bottom than in the equatorial plane [7].

The mean initial deuteron and triton densities are $n_D = n_T = 2.2 \times 10^{13}/\text{cm}^3$. The impurity species are α-particles, oxygen, and iron. The mean oxygen density is 1% of the mean initial hydrogen density $n_D + n_T$ and stays constant.

It is assumed that at the end of the flat top phase the current in the primary

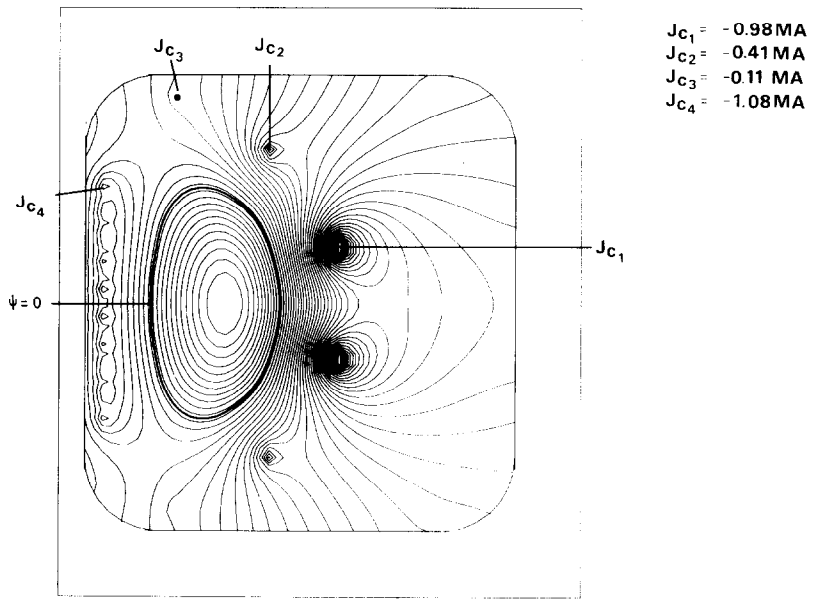

FIG. 9. Flux function inside and outside the JET-plasma. The Legendre representation of Eq. (7.8) accounts for the transformer iron. The plasma parameters are those of the flat top phase.

solenoid approaches its maximum value, which is compatible with the prescribed plasma shape. Therefore JET is treated as closed configurations, i.e., as the limiting case of the mixed configurations discussed in Section 5.3. To show that by the methods of Section 5.2 the prescribed plasma boundary can be obtained almost exactly, the currents in the groups g_1–g_4 were adjusted independently, therefore having two degrees of freedom more available than in reality. We note that in the early phase of the discharge the treatment as closed configuration is quite unrealistic.

Figure 9 shows the flux function at $t = 4.9$ s (flat top phase) generated by the coil groups g_1–g_4, and the plasma current and the transformer iron (Legendre representation; $N_L = 30$). A comparison with a vacuum calculation shows that the influence of the outer limbs on J_{c_1} is small because of the geometric dependence of μ_r and that of the iron core on J_{c_4} is small as well because of its saturation ($\mu_r \approx 2$). The currents $J_{c_{2,3}}$ changes are stronger because of the mirror current density in the upper and lower limbs. Their relative changes are 20% and 65%, respectively. The maximum temperature during the flat top phase due to additional heating are $T_{e_{\max}} = 8.7$ keV and $T_{i_{\max}} = 10$ keV. The total fusion power is $P_\alpha = 4.4$ MW (12% of the total input power). The time evolution of the stability parameters D_I and D_R investigated for the flux surface $\psi = 0.2\psi_{\min}$, i.e., in the vicinity of the plasma boundary, agrees almost exactly with the results given in Ref. [38]. There the analogous fixed boundary value problem was envisaged. The impurity content may be characterized by $Z_{\text{eff}_{\max}} = 3$.

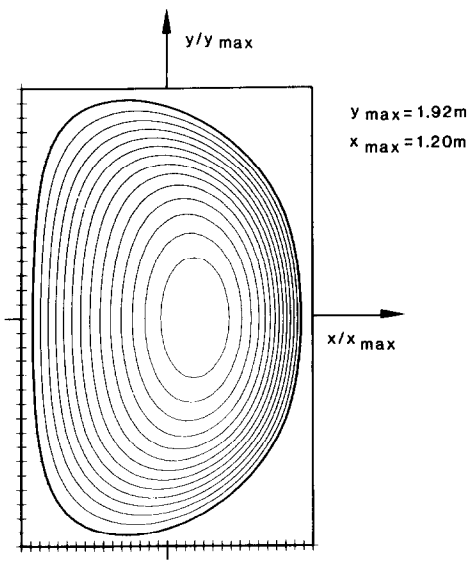

FIG. 10. Flux function inside the INTOR plasma boundary. The analytical expression (3.4) was chosen to describe the boundary.

The plasma current, the effective radius, and the elongation belonging to shot 6296 are given by $I_p = 2.42$ MA, $\rho_p = 1.42$ m, $\varepsilon = 1.35$, respectively. The excentricity is equal to unity and the D-shapeness is $d = 1.2$. The maximum temperatures are $T_{e\max} = 3.1$ keV and $T_{i\max} = 2.1$ keV; the maximum ion density is $n_{1\max} = 2 \cdot 10^{13}/\text{cm}^3$. Two coil groups, g_1 and g_4, are used to reproduce the currents $I_{ex_1} = 0.54$ MA and $I_{ex_4} = 0.68$ MA ($I_{ex_2} = I_{ex_3} = 0$). The maximum deviation is 4% only.

However, because of the attraction by the yokes, the plasma elongation was to be limited artifically by introducing a lower limit $C_\psi = 10^{-4}$ Vs of the flux function at the upper and lower side of the box in Fig. 2 thus partly employing the boundary condition of the fixed boundary value problem. The procedure corresponds roughly to a confining current distribution on the top and bottom of the box. This might simulate the action if a vessel's current distribution is possibly induced during earlier phases of the discharge.

10.3. *INTOR*

The INTOR design of Ref. [27] resorts to a poloidal divertor to achieve the particle and energy exhaust. The divertor might be also needed to reach the eventually decisive *H*-mode. Until now, however, it is not quite clear if a divertor device is more advantageous than a (pump) limiter device using the total available volume in the main vacuum vessel for the plasma operation. Although a divertor multipole could be included in the modelling, here the limiter case is treated, thereby concentrating on the fixed boundary value problem. The data of the INTOR-like device [27] read: $\rho_p = 151.8$ cm, $R_0 = 5.30$ cm, ellipticity $\varepsilon = 1.6$, excentricity $e = 2.13$, D-shape $d = 1.1$, toroidal field $B_{t_0} = 55$ kG, plasma current $J_p = 6.4$ MA. The plasma boundary is described by the analytical expression (3.4).

The data for additional heating, NI, and ICRH, are: beam turn-on time $t_{B_1} = 0$,

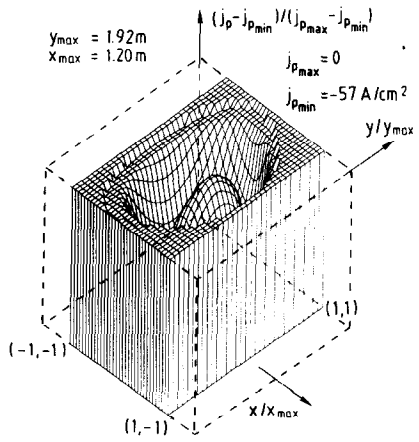

FIG. 11. Distribution of the poloidal current density in the burning INTOR plasma. The negative sign of this current density demonstrates the diamagnetism of the plasma.

beam turn-off time $t_{B_2} = 5$ s, beam power $P_B = 20$ MW, beam energy $E_B = 175$ keV, ICRH turn-on time $t_{I_1} = 1$ s, ICRH turn-off time $t_{I_2} = 5$ s. The fractions of P_B for the E_B, $E_B/2$, and $E_B/2$ components, and geometrical injector data are the same as in the JET-calculations. The injected species is deuterium and co-injection is assumed. The mean initial deuteron and triton densities are $n_0 = n_T = 7 \times 10^{13}/\text{cm}^3$. The ICRH power is $P_{RF} = 40$ MW. The impurity species are α-particles, oxygen, and iron.

After the startup phase (5 s) the temperature control is switched on so that the maximum temperatures stay approximately constant ($T_{e\max} = T_{i\max} = 20$ keV). The electron power balance shows that P_{α_e} is lost mainly by conduction and radiation. The ions are heated by fusion ($P_{\alpha_i} = 15$ MW). This power is almost removed by convection and the unloading process for stabilizing the temperature. A detailed analysis of the spectra of the emanating neutrals is given in Ref. [23]. These spectra had been taken as a basis to compute the evolution of the tritium density in the first wall of INTOR.

The poloidal flux function during the burn phase is shown in Fig. 10. The Shafranov shift is $d = 31$ cm. Due to the comparatively high pressure gradient the diamagnetism becomes important and the poloidal current density (Fig. 11) is negative everywhere. At the magnetic axis a peak arises due to the condition that the poloidal current density has to vanish there.

However, the maximum diamagnetic reduction for the toroidal field is only 2.2 kG. In the analogous JET case the poloidal current density is negative at the plasma boundary and in the vicinity of the plasma center only, thus providing an example of a partly paramegnetic and partly diamagnetic plasma. The ohmically heated TEXTOR plasma is paramagnetic everywhere.

Concluding Remarks

The results demonstrate that the combined code provides the possibility to describe the interaction between the confining magnetic field and the particle and energy inventory of a Tokamak plasma. In particular, the time evolution of equilibria can be computed on the rigorous basis proposed by Shafranov *et al.* [6]. Some aspects of plasma confinement, i.e., the computation of the coil currents maintaining the plasma equilibrium during the time evolution of the discharge can be treated in a rather general and straightforward way. This applies to all coil configuration of limiter Tokamaks. The extension to divertor configurations is possible and means in essence that some of the coil groups must be replaced by divertor multipoles to control the position of the x-points. To estimate the voltages driving the coil currents, the circuit data and the time dependence of the flux function at the coil positions can be employed. These voltages could be used as input for the free boundary problem discussed in Section 6; almost the same plasma shape and position as in the case of the semifree boundary value problem should be obtained, thus providing a valuable check.

However, one of the main tasks in tokamak physics, to understand the energy confinement on the basis of a stability analysis with respect to ideal and resistive MHD modes is not envisaged here in detail as it was attempted by other authors already [3, 53]. It remains as an important task to use the equilibrium information for a mode analysis and to adjust the confinement properties accordingly.

ACKNOWLEDGMENTS

The authors thank H. Kever for helpful discussions, Mrs. Hoffman for deciphering and typing the manuscript and Mrs. Biermann for the drawings. They are gratefully indebted to D. B. Nelson, H. C. Howe, E. C. Crume, and D. E. Post, whose codes have been the basis for the development of the "equilibrium," the "plasma," the "impurity," and the "neutral gas" modules used here. They especially thank J. T. Hogan for the comments concerning his "1 $\frac{1}{2}$ D"-procedure in the Oak Ridge Tokamak Transport code.

REFERENCES

1. F. L. HINTON AND R. D. HAZELTINE, *Rev. Mod. Phys.* **48**, 239 (1976).
2. H. GRAD, P. N. HU, AND C. STEVENS, *Proc. Nat. Acad. Sci. USA* **72**, 3789 (1975).
3. J. T. HOGAN, *Nucl. Fusion* **19**, 753 (1979).
4. H. GRAD AND J. HOGAN, *Phys. Rev. Lett.* **24**, 1397 (1970).
5. J. T. HOGAN, Oak Ridge National Laboratory, Tennessee, Report No. ORNL/TM-6049, 1978 (unpublished).
6. V. O. SHAFRANOV, G. V. PEREVERSEV, AND L. E. ZAKHAROV, in *Proceedings, 3rd Int. Conf. Plasma Theory, Kiev, Trieste*, 1977, p. 469.
7. J. BLUM AND J. LEFOLL, Laboratoire d'analyse numérique de Paris IV, Paris, France, Report No. EUR-CEA-FC-1029, 1983 (unpublished).
8. R. LÜST AND A. SCHLÜTER, *Z. Naturforsch.* **12a**, 850 (1957).
9. K. LACKNER, *Comput. Phys. Commun.* **12**, 33 (1976).
10. O. DE BARBIERE, D. F. DÜCHS, P. GAUTIER, K. LACKNER, G. G. LISTER, AND W. SCHNEIDER, The NET Team, Report, No. EUR XII 342/32, 1984 (unpublished).
11. B. COPPI, R. DAGAZIAN, AND R. GAJEWSKI, *Phys. Fluids* **13**, 2405 (1972).
12. L. L. LAO, S. P. HIRSHMANN, AND R. M. WIELAND, *Phys. Fluids* **24**, 1431 (1981).
13. W. A. HOULBERG, S. E. ATTENBERGER, AND L. M. HIVELY, *Nucl. Fusion* **22**, 935 (1982).
14. J. T. HOGAN, "Multifluid Tokamak Models," in Methods in Computational Physics Vol. 16, edited by J. Killeen (Academic Press, New York, 1976).
15. J. K. MUNRO, JR., J. T. HOGAN, H. C. HOWE, AND D. E. ARNURIUS, Oak Ridge National laboratory, Tennessee, Report No. ORNL/TM-5262, 1977 (unpublished).
16. D. F. DÜCHS, D. E. POST, AND P. H. RUTHERFORD, *Nucl. Fus.* **17**, 565 (1977).
17. D. E. POST, C. E. SINGER, AND A. M. KENNEY, private communication (1979).
18. J. T. HOGAN, *Nucl. Fus.* **21**, 365 (1981).
19. C. MERCIER, F. WERKOFF, J. P. MORERA, G. CISSOKO, AND H. CAPES, *Nucl. Fus.* **21**, 291 (1981).
20. K. AUDENAERDE, G. A. EMMERT, AND M. GORDINIER, Department of Nuclear Engineering, University of Wisconsin, Madison, Wisconsin, Report No. UWFDM-259, 1978 (unpublished).
21. M. H. HUGHES AND D. E. POST, *J. Comput. Phys.* **28**, 43 (1978).
22. D. REITER AND A. NICOLAI, *J. Nucl. Mater.* **111/112**, 434 (1982).
23. A. NICOLAI AND D. REITER, *J. Comput. Phys.* **55**, 129 (1984).
24. H. C. HOWE, *J. Nucl. Mater.* **93/94**, 17 (1980).
25. F. WAELBROECK, P. WIENHOLD, AND J. WINTER, *J. Nucl. Mater.* **111/112**, 185 (1982).
26. O. BUNEMAN, Stanford University Report No. SUIPR 294, 1969 (unpublished).
27. The INTOR group, *Nucl. Fus.* **22**, 135 (1982).

28. Kernforschungsanlage Jülich, Institut für Plasmaphysik, Assoziation Euratom-KFA, West Germany, The TEXTOR Team, Report on the Planning of TEXTOR, 1975 (unpublished).
29. K. KUPFMÜLLER, *Einführung in die theoretische Elektrotechnik* (Springer-Verlag, Berlin/Göttingen/Heidelberg, 1962), p. 234.
30. C. SCHÄFER, *Einführung in die theoretische Physik*, 3rd volume (de Gruyter, Berlin, 1950), p. 126.
31. W. ENGELHARDT, K. BEHRINGER, AND G. FUSSMANN, in *Verhandlungen der Deutschen Physikalischen Gesellschalft, Hamburg March* 23, 1981.
32. V. E. GOLANT, Plasma Physics and Contr. Fus. **26**, 77 (1984).
33. Y.-K.M. PENG, Oak Ridge National Laboratory, Report No. ORNL, FEDC-84/7, 1984 (unpublished).
34. H. SOLTWISCH, H. L. BAY, G. BERTSCHINGER, P. BOGEN *et al.*, *Plasma Phys. Controlled Fusion* **26**, 23 (1984).
35. The JET project, Culham, England, Report No. EUR-JET-R5, 49, 1975 (unpublished).
36. M. L. WATKINS, The JET Project, Culham, England, private communication (1981).
37. M. BRUSATI, A. GIBSON, AND J. R. LAST, The JET Project, Culham, England, private communication (1986).
38. A. NICOLAI AND D. REITER, in *Proceedings, Eleventh European Conf. on Controlled Fus. and Plas. Phys., Aachen, West Germany*, 1983, Vol. II, p. 295.
39. S. P. HIRSHMANN AND D. J. SIGMAR, *Nucl. Fusion* **21**, 1079 (1981).
40. H. L. BAY, J. ROTH, AND J. BODHANSKY, *J. Appl. Phys.* **48**, 4722 (1977).
41. R. V. JENSEN, D. E. POST, W. H. GRASBERGER, C. B. TARTER, AND W. A. LOKKE, *Nucl. Fusion* **17**, 1187 (1977).
42. R. H. FOWLER AND J. A. ROME, Oak Ridge National Laboratory, Tennessee, Report No. ORNL 6845, 1979 (unpublished).
43. J. A. ROME, D. G. MCALEES, R. H. FOWLER, AND J. D. CALLEN, *Nucl. Fusion* **16**, 55 (1976).
44. J. D. CALLEN, Oak Ridge National Laboratory, Tennessee, private communication (1979).
45. K. BORASS, K. LACKNER, AND E. MINARDI, in *Proceedings, Ninth European Conference on Controlled Fusion and Plasma Physics, Oxford, England*, 1979, p. 110.
46. G. REQUIN, B. GAGEY, J. P. GIRARD, AND A. SAMAIN, in *Proceddings, Second Joint Grenoble–Varenna International Symposium COMO, Italy*, 1980, p. 1178.
47. A. NICOLAI AND G. FUCHS, in *Proceedings, Eigth European Conference on Controlled Fusion and Plasma Physics, Prague, Czechoslovakia*, 1977, p. 26.
48. A. NICOLAI AND G. FUCHS, *J. Nucl. Mater.* **76/77**, 556 (1978).
49. G. FUCHS AND A. NICOLAI, *Nucl. Fusion* **20**, 1247 (1980).
50. A. NICOLAI AND P. BÖRNER, *J. Nucl. Mater.* **145-147**, 873 (1987).
51. R. G. BATEMAN, *MHD Instabilities* (MIT Press, Cambridge, MA/London, 1978), p. 130.
52. B. CARRERAS, H. R. HICKS, AND B. V. WADELL, *Nucl. Fusion* **19**, 583 (1979).
53. H. R. HICKS, B. CARRERAS, J. H. HOLMES, D. K. LEE, AND B. V. WADELL, *J. Comput. Phys.* **44**, 46 (1981).
54. B. COPPI AND E. MAZZUCATO, *Phys. Lett. A* **71**, 337 (1979).
55. A. B. BERLIOZ, V. I. BUGARYA, V. V. BUZANKIN, N. L. VASIN, A. N. VERTIPOROKH *et al.*, in *Proceedings, Eigth Intl. Conference on Plasma Physics and Controlled Nuclear Fusion Research* 1980, *Brussels, Belgium*, 1980, Vol. I (IAEA, Vienna, 1981), p. 23.
56. A. NICOLAI AND G. H. WOLF, *in Proceedings, Eleventh European Conf. on Controlled Fusion and Plasma Phys., Aachen, West Germany*, 1983, p. 319.
57. F. TROYON, R. GRUBER, H. SAUREMANN *et al.*, *Plasma Phys. Controlled Fusion* **26**, 209 (1984).
58. R. G. BATEMAN, Oak Ridge National Laboratory, Tennessee, private communiation (1979).
59. K. YAMAZAKI, T. AMANO, H. NAITOV, Y. HAMADA, AND M. AZUMI, *Nucl. Fusion* **25**, 1543 (1985).
60. B. B. KADOMTSEV, *Plasma Phys. Controlled Fusion* **26**, 217 (1984).
61. F. ALLADIO, E. BARBOTO, G. BARTIMORO *et al.*, in *Proceedings, Eleventh Conf. on Controlled Fusion and Plasma Phys., Aachen, West Germany*, 1983, p. 27.
62. M. KEILHACKER, in *Proceedings, IAEA Technical Committee Meeting on Divertors and Impurity Control, Garching, West Germany*, 1981, p. 23.